

Article

Estimation of Aboveground Biomass for Different Forest Types Using Data from Sentinel-1, Sentinel-2, ALOS PALSAR-2, and GEDI

Chu Wang ¹, Wangfei Zhang ¹, Yongjie Ji ^{2,*}, Armando Marino ³, Chunmei Li ⁴, Lu Wang ², Han Zhao ¹ and Mengjin Wang ¹

¹ College of Forestry, Southwest Forestry University, Kunming 650224, China; wangchu@swfu.edu.cn (C.W.); zhangwf@swfu.edu.cn (W.Z.); zhan98gisrs@swfu.edu.cn (H.Z.); wmj@swfu.edu.cn (M.W.)

² School of Geography and Ecotourism, Southwest Forestry University, Kunming 650224, China; wanglu8008@swfu.edu.cn

³ Biological and Environmental Sciences, The University of Stirling, Stirling FK9 4LA, UK; armando.marino@stir.ac.uk

⁴ China Spacesat Co., Ltd., Beijing 100081, China; lichunmeizgwx@spacechina.com

* Correspondence: jiyoungjie@live.cn

Abstract: Forest aboveground biomass (AGB) is integral to the global carbon cycle and climate change study. Local and regional AGB mapping is crucial for understanding global carbon stock dynamics. NASA's global ecosystem dynamics investigation (GEDI) and combination of multi-source optical and synthetic aperture radar (SAR) datasets have great potential for local and regional AGB estimation and mapping. In this study, GEDI L4A AGB data and ground sample plots worked as true AGB values to explore their difference for estimating forest AGB using Sentinel-1 (S1), Sentinel-2 (S2), and ALOS PALSAR-2 (PALSAR) data, individually and in their different combinations. The effects of forest types and different true AGB values for validation were investigated in this study, as well. The combination of S1 and S2 performed best in forest AGB estimation with R^2 ranging from 0.79 to 0.84 and RMSE ranging from 7.97 to 29.42 Mg/ha, with the ground sample plots used as ground truth data. While for GEDI L4A AGB product working as reference, R^2 values range from 0.36 to 0.47 and RMSE values range from 31.41 to 37.50 Mg/ha. The difference between using GEDI L4A and ground sample plot as reference shows obvious dependence on forest types. In summary, optical dataset and its combination with SAR performed better in forest AGB estimation when the average AGB is less than 150 Mg/ha. The AGB predictions from GEDI L4A AGB product used as reference underperformed across the different forest types and study sites. However, GEDI can work as ground truth data source for forest AGB estimation in a certain level of estimation accuracy.



Citation: Wang, C.; Zhang, W.; Ji, Y.; Marino, A.; Li, C.; Wang, L.; Zhao, H.; Wang, M. Estimation of Aboveground Biomass for Different Forest Types Using Data from Sentinel-1, Sentinel-2, ALOS PALSAR-2, and GEDI. *Forests* **2024**, *15*, 215. <https://doi.org/10.3390/f15010215>

Academic Editor: Russell G. Congalton

Received: 23 November 2023

Revised: 17 December 2023

Accepted: 17 January 2024

Published: 21 January 2024

Corrected: 20 February 2024



Copyright: © 2024 by the authors. Licensee MDPI, Basel, Switzerland. This article is an open access article distributed under the terms and conditions of the Creative Commons Attribution (CC BY) license (<https://creativecommons.org/licenses/by/4.0/>).

1. Introduction

Forest is one of the most important ecosystems on Earth. It plays a vital role in mitigating climate change through absorbing a significant amount of carbon dioxide and releasing oxygen. Forest also serves as critical water sources, which contribute to water cycle maintenance and water quality [1,2]. Forest ecosystems play a crucial role in global carbon cycling and climate change [3], and they significantly influence changes in carbon dioxide. Accurate estimation of forest biomass at large regional scales enables accurate monitoring of global carbon stock changes and global climate changes [4–6]. Traditional forest inventory sampling is a well-established method for estimating biomass over the past decades. However, this method is constrained by high costs and spatial limitations. With the development of remote sensing technology, previous studies explored biomass estimation at a regional level by combining remote sensing techniques with field surveys. Compared

to traditional methods, airborne laser scanning can accurately measure important indicators such as canopy height and profile information [7]. However, it is also limited by regional estimation with high costs. With the launch and operation of the global ecosystem dynamics investigation (GEDI), a spaceborne lidar system, it becomes possible to acquire forest height and forest aboveground biomass (AGB) information regionally and globally. The introduction of the GEDI level 4A forest AGB product provides an alternative reference dataset for areas where field inventories are not possible. Meanwhile, ground truth data replaced by GEDI level 4A products may be more economical and convenient for regional and global forest AGB and carbon storage estimation [8,9].

In recent years, significant progress has been made for spatially continuous forest AGB mapping through the combination of different data sources, like combinations of synthetic aperture radar (SAR) data and optical remote sensing data. SAR, with its higher penetration capability, can penetrate clouds and fog and enables the continuous monitoring and acquisition of forest information [10,11]. Optical data, which are mostly free and available with global coverage, were reported to serve as reliable predictors for AGB estimation in various forest types. It currently became a frequently used data source with low-cost, large-scale, and high-precision for forest AGB estimation and mapping [12,13]. SAR data can provide information on forest vertical structure to a certain extent [14], while optical multi-spectral data can give more texture and horizontal information of forest [15]. To obtain forest AGB at regional scales, combining SAR data and optical data provides great potential for obtaining accurate forest AGB estimation [16–18]. Previous studies explored forest AGB estimation using a combination of optical and SAR datasets; however, most of the performance is based on training and validating the inversion model using field-collected samples [19,20]. The capability of using GEDI level 4A product of forest AGB as ground truth substitute data and the difference compared with using field-collected samples as ground truth data were not fully explored. Moreover, the influence of forest types on using GEDI level 4A product of forest AGB as ground truth data during the forest AGB estimation was not addressed yet.

According to the above mentioned research gaps, this study aims to evaluate the accuracy of forest AGB estimation in Yunnan Province using both GEDI L4A data and field measurements as ground truth data with optical data, SAR data, and combination of optical and SAR data sources. The following aspects will be addressed in this study: (1) To explore the capability of forest AGB estimation using single optical dataset, single SAR dataset, and a combination of optical and SAR datasets. (2) To assess the difference between using GEDI L4A data and field measurements as ground truth for forest AGB estimation through different data sources. (3) To estimate the influence of forest types and test sites on the prediction accuracy of forest AGB.

2. Materials and Methods

2.1. Study Area Overview and Field Campaign

Two study areas located in Yunnan Province ($97^{\circ}31' - 106^{\circ}11'$ E; $21^{\circ}08' - 29^{\circ}15'$ N) were considered in this study (Figure 1). Yunnan Province, located at the junction of South Asia and Southwest China, shares borders with Myanmar, Laos, and Vietnam. It serves as a gateway for cross-border openness and is an important region for the construction of the “Belt and Road” ecological community [21–23]. The study area of Yiliang is located in the central part of Yunnan Province, which is located in the Xiaoshao forest farm of Yiliang County, Kunming ($24^{\circ}30'36'' - 25^{\circ}17'02''$ N; $102^{\circ}58'22'' - 103^{\circ}28'75''$ E). The altitude of Yiliang County ranges from 1300 m to 2500 m, and the climate belongs to the north subtropical monsoon climate, with an average annual temperature of 17.2°C . It is rainy in summer and fall, with an average annual precipitation of 956.7 mm. The study area of Pu'er is located in the southern part of Yunnan Province, and most of the samples collected are in the Wanzhangshan forest farm ($22^{\circ}27' - 23^{\circ}06'$ N; $100^{\circ}19' - 101^{\circ}27'$ E). The altitude of the study area ranges from 578 m to 2155 m. The average temperature is 18.9°C and the

average annual precipitation is 1487.5 mm. The main forest types in the two study areas are coniferous forest and broadleaf forest.

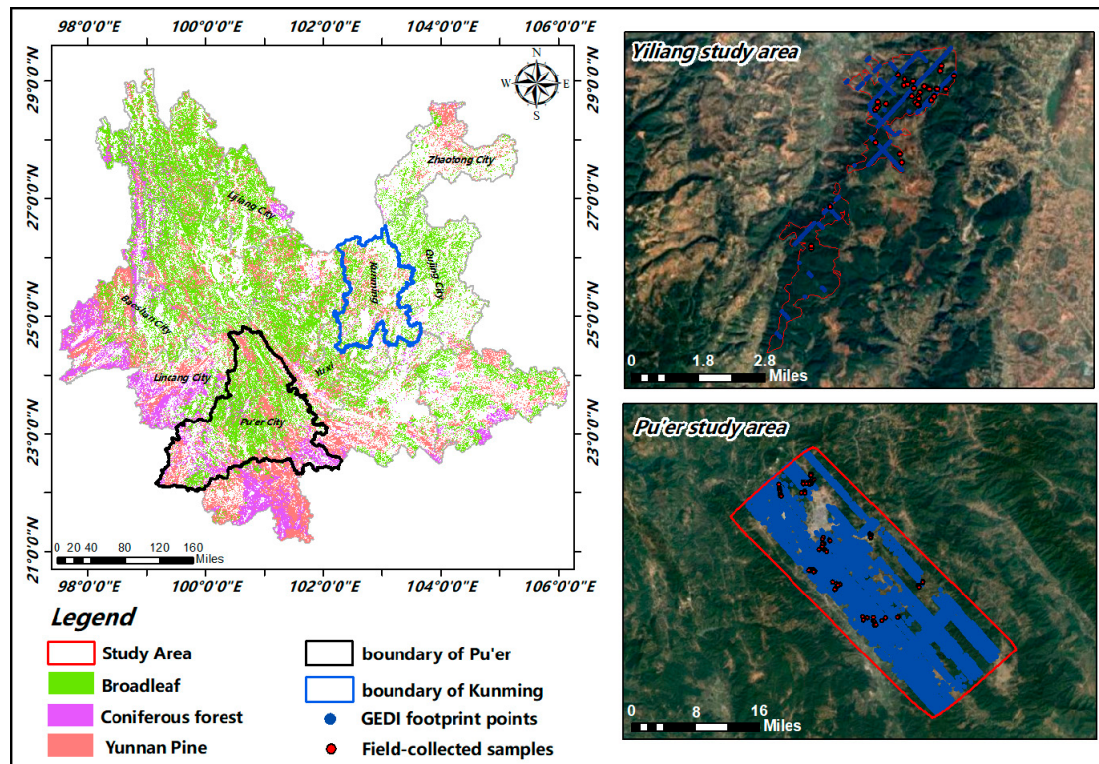


Figure 1. Location map of the study areas in Yunnan Province, Southwest of China. The left sub-panel shows the county locations of two study areas in Yunnan Province, the background is the forest types product. The edge of Kunming, where Xiaoshao farm is located, is in blue color while the edge of Pu'er, where Pu'er study area is located, is in black color. The top-right-sub-panel shows the boundary (red line) of Xiaoshao farm and the distribution of ground-collected samples (red points) and GEDI footprint points (blue points). The bottom-right-sub-panel shows the boundary (red line) of Pu'er test site and the distribution of ground-collected samples (red points) and GEDI footprint points (blue points).

2.1.1. Pu'er Study Area

Ground surveys were conducted in December 2020 in Pu'er. A total of 27 coniferous forest plots ($20 \text{ m} \times 20 \text{ m}$) and 31 broadleaf forest plots ($20 \text{ m} \times 20 \text{ m}$) were collected in this study area. The dominated tree species in coniferous forest is Simao pine (*Pinus kesiya*). The locations of four corner points and a central point of each square plot were georeferenced by a differential global positioning system (GPS). Diameter at the breast height (DBH, DBH at 1.3 m height) and tree height were collected with trees having DBH greater than or equal to 5 cm. The AGB values of each tree were calculated and totaled to obtain the AGB total amount for all trees in each plot, then the area of each sample plot was divided to obtain the total AGB of each sample plot.

2.1.2. Yiliang Study Area

A total of 40 coniferous forest plots were surveyed in the Yiliang study area with the angle count method [24]. The dominated tree species here is Yunnan pine (*Pinus yunnanensis*). All trees with a DBH greater than 5 cm were recorded. GPS coordinates of the observation point for each plot, DBH measurements of counted trees, tree height, and horizontal distance from the tree trunk center to the observation point were collected. The AGB of each sample plot was obtained through the following steps through two steps: first,

the volume per hectare was calculated for each plot, and then the conversion from volume to AGB was performed later [25].

Table 1 shows the related forest detail information of the two study areas. The canopy projection method was used to calculate the average crown cover and the percentages were recorded. The equations of AGBs for tree species involved in two study areas were calculated using the equations presented in Table 2 [26].

Table 1. Statistics for the forest information of two study areas.

Study Area	Forest Type	Number of Plots	AGB (Mg/ha)	Average AGB (Mg/ha)	Average Crown Cover (%)
Pu'er	Coniferous forest	27	69.61–162.30	120.89	70.00
	Broadleaf forest	31	73.26–288.68	141.68	75.46
Yiliang	Coniferous forest	40	9.34–78.51	36.13	63.00

Table 2. Forest biomass equations for each tree species in two study areas.

Tree Species	Biomass Model
Simao Pine (<i>Pinus kesiya</i>)	$M = 0.0582DBH^{0.4668}$
Chinese Gugertree (<i>Schima superba</i>)	$M = 0.12045DBH^{2.06446}H^{0.38265}$
Farges's Chinkapin (<i>Castanopsis fargesii</i>)	$M = 0.1355(DBH^2H)^{0.817} + 0.0275(DBH^2H)^{0.8166}$
Blue Gum (<i>Eucalyptus globulus</i>)	$\lg M = 0.814\lg(DBH^2H) - 0.9816$
Weeping Cypress (<i>Cupressus funebris</i>)	$M = 0.010158DBH^{2.94424}H^{0.41591}$
Chinese Fir (<i>Cunninghamia lanceolata</i>)	$M = 0.10301(DBH^2H)^{0.7773}$
Other broadleaf species	$M = 0.3507(DBH - 1.1948)^2 + (0.03017DBH^{2.3643} + 0.051) + (0.01813DBH^2 - 0.2477)$ (Hard and wide category)
Yunnan Pine (<i>Pinus yunnanensis</i>)	$V = F_g \sum_{i=1}^k Z_j(fh)_i; M = 0.08596V^{0.8564}$

DBH is the diameter at breast height, H is the height of the tree, and M is the AGB of each tree; V is the stem volume, F_g is the basal area factor, Z_j is the number of trees at diameter class of j , $(fh)_i$ is the form height at diameter class of i .

2.2. Satellite Data

Sentinel-2 (S2) optical data, SAR data including C-band Sentinel-1 (S1), and L-band ALOS PALSAR-2 were used in this study for remote sensing independent variable extraction. S1, one of a series of radar satellites operated by the European Space Agency (ESA), is used for Earth observation and environmental monitoring. It was equipped with a C-band SAR sensor with a wavelength of approximately 5.8 cm. PALSAR-2 is a radar satellite launched by the Japan Aerospace Exploration Agency (JAXA) and it is used for Earth observation and environmental monitoring. The PALSAR-2 satellite carries an L-band SAR sensor, which operates at a longer wavelength (approximately 23.5 cm) and exhibits strong penetration of forest canopy structure [27].

In this study, all SAR data were collected during the plant growth period from April to October of 2020 for Pu'er and from April to October of 2019 for Yiliang. All of these datasets were collected and processed through the Google Earth Engine (GEE) platform (<https://earthengine.google.com/>, accessed on 22 September 2023). The features extracted from the SAR datasets are shown in Table 3.

Table 3. SAR data modeling factor information.

Variable Type	Variable Name	Definition
Polarization Information	VV, VH	Backscatter coefficients from S1
	HH, HV	Backscatter coefficients PALSAR-2
	VV-VH	Polarization Difference
Constructed features	VH+VV	Polarization Sum
	HH/HV	Polarization Ratio

S2 is one of a group of Earth observation satellites launched by the ESA with the aim of providing high-resolution, multi-spectral remote sensing data. The S2 satellite was equipped with a multi-spectral imager (MSI). The MSI sensor on S2 captures data in 13 spectral bands, including visible, near-infrared, and shortwave infrared bands. Each S2 satellite has an imaging width of 290 km, enabling wide coverage of the Earth's surface. Furthermore, the multiple satellites in the S2 series were operated on different orbits, providing more frequent data acquisition and faster revisit cycles. In this study, all S2 datasets were acquired from April to October in 2020 for Pu'er and in 2019 for Yiliang. They were preprocessed on the GEE platform, as well. Vegetation indices extracted from S2 and their calculation equations are shown in Table 4.

Table 4. Vegetation index calculation equation.

Vegetation Index	Calculation Formula	Reference
Normalized difference vegetation index (NDVI)	$NDVI = \frac{\rho_{NIR} - \rho_{red}}{\rho_{NIR} + \rho_{red}}$	[28]
Green and red vegetation index (GRVI)	$GRVI = \frac{\rho_{green} - \rho_{red}}{\rho_{green} + \rho_{red}}$	[28]
Leaf area index (LAI)	$LAI = 3.618 \times \frac{\rho_{NIR1} - \rho_{red}}{\rho_{NIR1} + \rho_{red} + 0.5}$	[29]
Differential vegetation index (DVI)	$DVI = \rho_{NIR} - \rho_{red}$	[28]
Infrared-red enhanced vegetation index (IRECI)	$IRECI = \frac{\rho_{RE3} - \rho_{red}}{\rho_{RE3}} \times \rho_{RE2}$	[30]
Ratio vegetation index (RVI)	$RVI = \rho_{NIR} / \rho_{red}$	[28]
MERIS terrestrial chlorophyll index (MTCI)	$MTCI = \frac{\rho_{RE2} - \rho_{RE1}}{\rho_{RE1} - \rho_{red}}$	[30]
Atmospheric resistance vegetation index (ARVI)	$ARVI = \rho_{NIR} - \frac{(2 \times \rho_{red} - \rho_{blue})}{\rho_{NIR1} + (2 \times \rho_{red} - \rho_{blue})}$	[28]
Red-edge inflection point index (REIP)	$REIP = 700 + \frac{40 \times (\rho_{red} + \rho_{RE3})}{(\rho_{RE2} - \rho_{RE1}) \times (2 - \rho_{RE1})}$	[31]

RE1 has a wavelength of 698–713 nm, RE2 has a wavelength of 733–748 nm, and RE3 has a wavelength of 773–793 nm [32].

GEDI L4A data were downloaded from the Earth data platform of the National Aeronautics and Space Administration (NASA) at the same time period for two test sites <https://search.earthdata.nasa.gov/>, accessed on 23 September 2023). The GEDI LiDAR system consists of three lasers that generate eight parallel observation tracks. Each laser emits at a frequency of 242 Hz, and illuminates a 25 m footprint to measure a three-dimensional structure. The footprints are separated with a track of 60 m and a cross-track distance of 600 m. GEDI L4A provides estimates of AGB (Mg/ha) for each footprint based on a three-dimensional measured structure. Footprint AGB was derived from parametric models which relate simulated GEDI level 2A (L2A) waveform relative height (RH) metrics to field plot estimates of AGB. Height metrics from simulated waveforms associated with field estimates of AGB from multiple regions and plant functional types (PFTs) were compiled to generate a calibration dataset for models representing the combinations of world regions and PFTs [33].

2.3. Methodology

Individual remote sensing data sources (S1, S2, and PALSAR-2) and combinations of data sources (PALSAR + S2 and S1 + S2) were evaluated separately in this study. Pixel values were extracted for plot size (20 m × 20 m) and GEDI L4A footprint (25 m × 25 m). Four regression models were trained for four forest AGB estimation types, including

random forest (RF), K-nearest neighbor (KNN), gradient boosted regression tree (GBRT), and linear regression. A 10-fold cross-validation with an average of 10 repetitions was used to validate the estimation results. Field-collected samples and GEDI footprints of AGB products were used in this study as AGB references in the forest AGB estimation process. In order to adjust the pixel values from the different data sources to the plot size and the observed range of the GEDI foot points, we used a nearest neighbor resampling method to average the pixel values of the optical and SAR factor images according to the location of each plot and each GEDI foot point. After resampling, the spatial resolution is unified as 30 m. This operation helps to maintain data consistency and allows information from different data sources to be effectively compared and integrated at the same spatial scale. In the stage of extracting remote sensing features, considering the different properties of the S1, S2, and PALSAR-2 data, the block statistical analysis was conducted with the window sizes of 2, 2, and 1, respectively. The flowchart of this study is described in Figure 2.

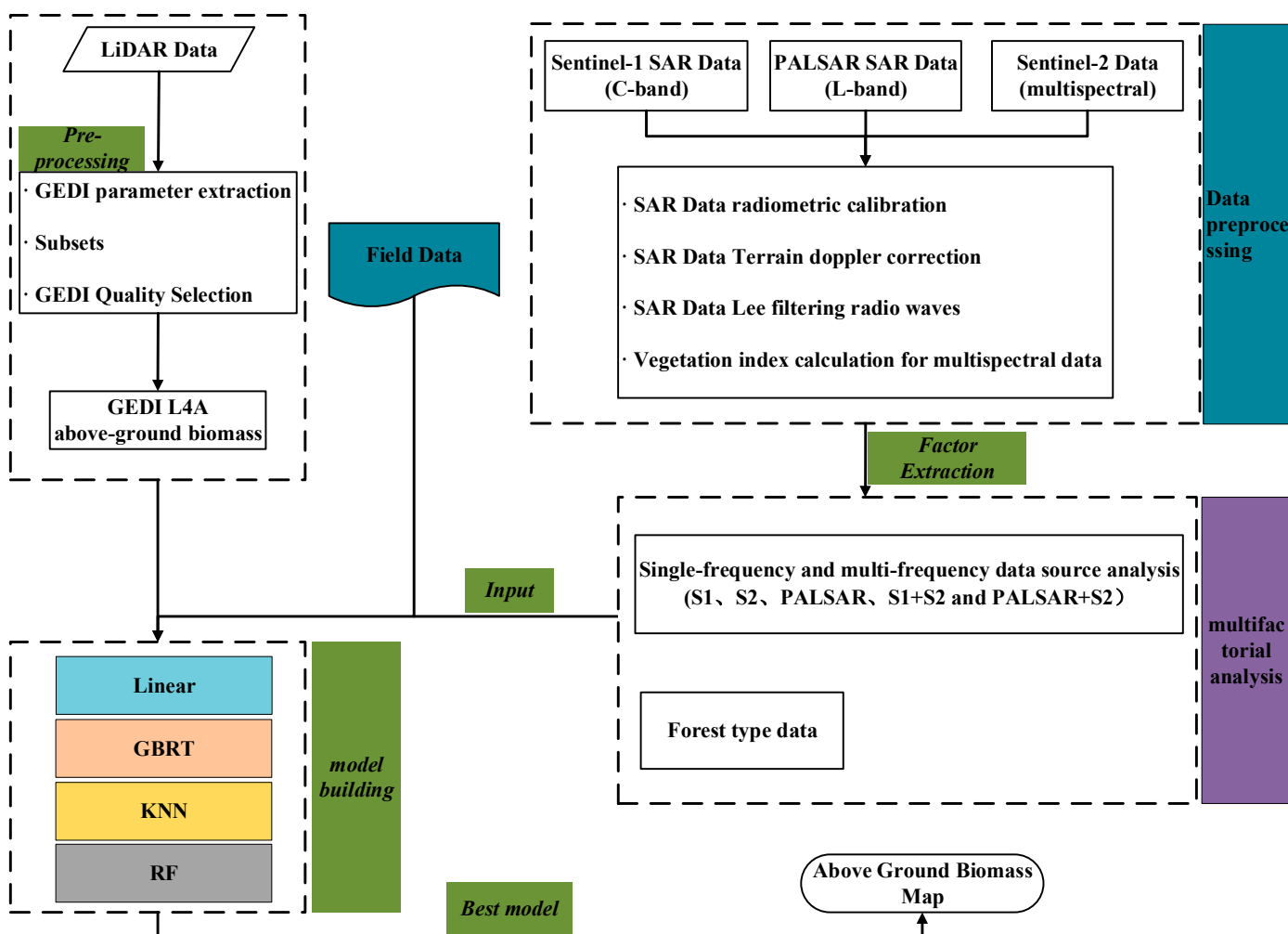


Figure 2. Flowchart of this study.

2.4. Model Evaluation

The predictive performance of each model was evaluated based on its R^2 (Equation (1)) and RMSE (Equation (2)) values. The model with the highest scores (higher R^2 and lower RMSE) was selected to generate the AGB map for the study areas.

$$R^2 = 1 - \frac{\sum_{i=1}^n (y_i - \hat{y}_i)^2}{\sum_{i=1}^n (y_i - \bar{y})^2} \quad (1)$$

$$RMSE = \sqrt{\frac{\sum_{i=1}^n (y_i - \hat{y}_i)^2}{n}} \quad (2)$$

where y_i is the observed AGB value at pixel i , \hat{y}_i is the estimate of AGB, n is the number of pixels in the field sample, and \bar{y} is the average AGB in the field plots.

In this study, an algorithm called “scikit-learn” package embedded in Python (version 3.8) was used for forest AGB estimation. The spatial mapping and analysis were mainly performed in ArcGIS (version 10.4.1), scattering plots and validation statistics were performed in Python (version 3.8) and Origin 2022.

The grid search algorithm (GS) divides the parameters to be searched into the grid with a certain spatial extent, and searches for the optimal parameters by traversing all points in the grid to obtain the global optimal solution [34]. In the training phase, the hyperparameters of the model are tuned using a grid search with cross-validation (CV = 10). The RF model contains four hyperparameters: the number of decision trees (`n_estimators`), the maximum depth of the decision trees (`max_depth`), the minimum number of samples in the leaf nodes (`min_samples_leaf`), and the minimum number of split samples (`min_samples_split`). The GS optimizes the remaining hyperparameters to obtain the hyperparameter values for each iteration. RMSE was chosen to measure the accuracy of the model during hyperparameter optimization [35,36]. In this study, after several hyperparameter optimization trainings, the best parameters of the model appeared before 50 iterations. After 50 iterations, the RMSE changed slightly and the accuracy of the model could not be improved any further. Therefore, the optimal hyperparameters are `n_estimators`: 50, `max_depths`: 20, `min_samples_leaf`: 1, `min_samples_splits`: 2. The GBRT model contains three hyperparameters, including `n_estimators`, `max_depths`, learning rate (`learning_rate`). The remaining hyperparameters are optimized by the GS to obtain the hyperparameter values for each iteration. When the GBRT model performs hyperparameter optimization, the RMSE is minimized and the model performs best in the 110th iteration. The optimal hyperparameters are `n_estimators`: 300, `max_depths`: 50, `learning_rate`: 0.05. For the KNN model, including the number of nearest neighbors (`n_neighbors`), weights, distance metric and algorithm for calculating the nearest neighbors, the grid is used to search for the optimal combination of these parameters and 10-fold cross-validation is used to evaluate the performance of each K-value, which ultimately returns the optimal combination of parameters and the corresponding optimal model [37–40]. The optimal hyperparameters are `n_neighbors`: 10, `weights`: uniform, `metric`: Euclidean, `algorithm`: auto.

3. Results

3.1. Performance of the Algorithm

Figure 3 shows the performance of the selected four models used for modeling forest AGB with five different combinations of three remote sensing data sources. According to the R^2 values, the RF model shows the best performance among all models, regardless of whether AGB values are based on GEDI L4A data or field measurements. At the plot level, the combination of optical and C-band SAR data exhibited the highest scores for the RF model ($R^2 = 0.80$; Figure 3a). When GEDI L4A data were used as a reference, the RF model also performed best ($R^2 = 0.45$; Figure 3a).

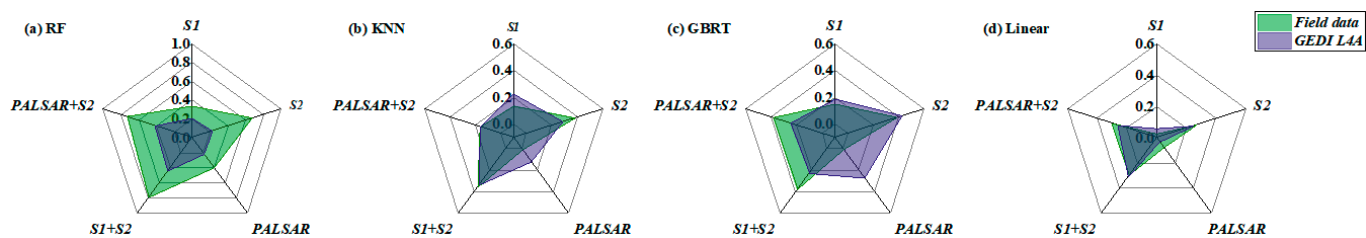


Figure 3. Radar charts for R^2 of the model performance using samples in two study areas with different combinations of remote sensing datasets (S1, S2, PALSAR, S1 + S2, PALSAR + S2). The different colors of the polygon indicate the use of different AGB reference sources (green for field data and purple for GEDI L4A).

Figure 4 shows that RF has the smallest prediction error on both AGB reference sources on average of each data combination. The smallest RMSE value was obtained when using the field data and the S1 + S2 combination ($RMSE = 29.41 \text{ Mg/ha}$; Figure 4a), whereas the same combination returned a relatively large error when using the GEDI data as the ground truth value ($RMSE = 35.78 \text{ Mg/ha}$; Figure 4a).

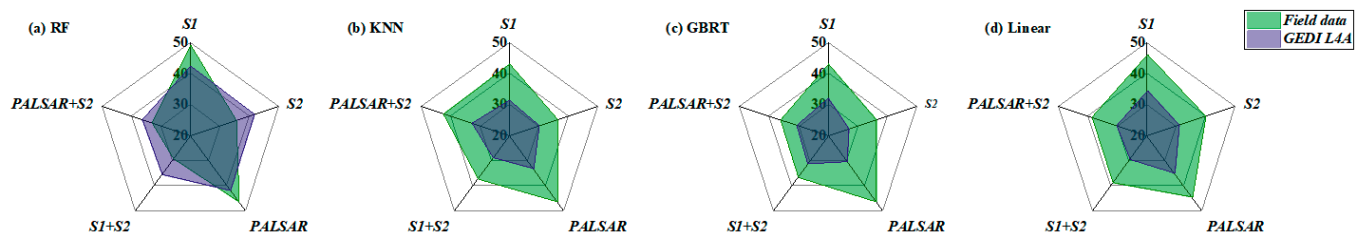


Figure 4. Radar charts for RMSE of the model performance using samples in two study areas with different combinations of remote sensing datasets (S1, S2, PALSAR, S1 + S2, PALSAR + S2). The different colors of the polygon indicate the use of different AGB reference sources (green for field data and purple for GEDI L4A).

3.2. Forest AGB Estimation for Whole Forest Type

Given the better performance of the RF algorithm in forest AGB estimation, RF was used here for forest AGB estimation over the whole forest types and for each single forest type. The performance on AGB prediction across the study areas of Yunnan Province with the whole forest type was assessed by plotting the measured values against the predicted values for each AGB reference source (Figure 5). Figure 5 demonstrates the best accuracy obtained using field-collected measurements as training and validation data. However, the RMSE difference using each data combination is no more than 10 Mg/ha. The AGB estimates generated using the field measurements as the AGB reference values show that the S1 + S2 combination performed best with $R^2 = 0.80$ and $RMSE = 29.42 \text{ Mg/ha}$ (Figure 5d). For the SAR data source, PALSAR data ($R^2 = 0.41$, $RMSE = 46.76 \text{ Mg/ha}$; Figure 5c) outperformed S1 ($R^2 = 0.34$, $RMSE = 49.36 \text{ Mg/ha}$; Figure 5a). When using the GEDI L4A product as the AGB reference, the C-band SAR data combined with optical data (S1 + S2, $R^2 = 0.45$, $RMSE = 35.78 \text{ Mg/ha}$; Figure 5i) still show better performance compared to the PALSAR data combined with optical data (PALSAR + S2, $R^2 = 0.42$, $RMSE = 36.59 \text{ Mg/ha}$; Figure 5j).

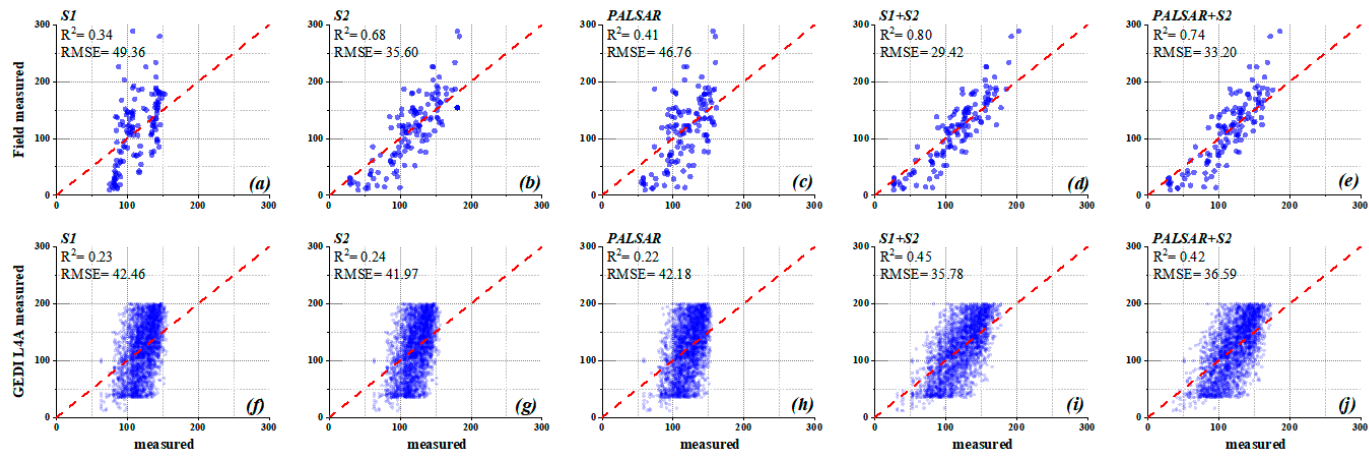


Figure 5. Relationships between measured and predicted AGB values for optical and SAR data for all forest types (all the samples in the two study areas) in the study area of Yunnan Province. The first row subfigures (a–e) use field measurements as the AGB reference, and the second row subfigures (f–j) use the GEDI L4A product as the AGB reference. The subfigures (a,f) are for Sentinel-1, the subfigures (b,g) are for Sentinel-2, the subfigures (c,h) are for PALSAR-2, the subfigures (d,i) are for Sentinel-1 and Sentinel-2, and the subfigures (e,j) are for PALSAR-2 and Sentinel-2.

3.3. Forest AGB Estimation for Different Forest Types

3.3.1. Broadleaf Forests

The study area was divided into different forest types and forest AGB was modeled separately for each type. Figure 6 describes the performance of five data combinations in forest AGB estimation results of broadleaf forests in Pu'er. In the broadleaf forests, using field measurements as a reference for AGB, the S1 + S2 combination shows the best fit ($R^2 = 0.83$, $RMSE = 12.54$ Mg/ha; Figure 6d), and when GEDI L4A data were used as a reference, the S1 + S2 combination ($R^2 = 0.47$, $RMSE = 35.54$ Mg/ha; Figure 6i) shows the best fit. With both field measurements and GEDI L4A as a reference, the single data source of S2 performed best in all three single data sources ($R^2 = 0.82$, $RMSE = 19.86$ Mg/ha; Figure 6b), even better than the performance of the combination of PALSAR + S2 ($R^2 = 0.78$, $RMSE = 26.84$ Mg/ha; Figure 6e). The results show that in broadleaf forests AGB estimation, no matter which biomass value worked as the reference value, C-band SAR data combined with optical data provide the best performance, and the model performance was improved by about 10%–20% on average. Note that the difference of $RMSE$ values using field measurements and GEDI L4A as reference was clearly improved when compared with whole forest types. The greatest difference was 23 Mg/ha using S1 + S2 and the lowest difference was 5.91 Mg/ha using S2 (Figure 6e,j).

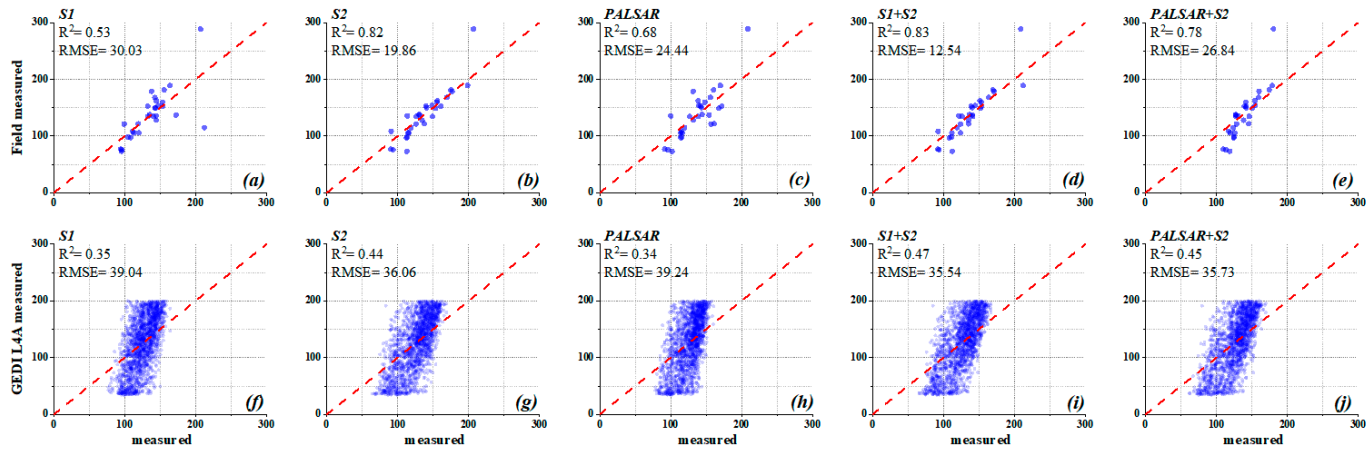


Figure 6. Relationship between measured and predicted AGB values for broadleaf forests in the Pu'er study area. The first row subfigures (a–e) uses field measurements as the AGB reference, and the second row subfigures (f–j) uses the GEDI L4A product as the AGB reference. The subfigures (a,f) are for Sentinel-1, the subfigures (b,g) are for Sentinel-2, the subfigures (c,h) are for PALSAR-2, the subfigures (d,i) are for Sentinel-1 and Sentinel-2, and the subfigures (e,j) are for PALSAR-2 and Sentinel-2.

3.3.2. Coniferous Forests in Pu'er

In the AGB estimation for coniferous forests in Pu'er where the dominated tree species is *Simao pine* (Figure 7), the combinations of both S1 and PALSAR with S2 performed better than single data sources. The highest score was acquired by S1 + S2 ($R^2 = 0.79$, $RMSE = 25.21$ Mg/ha; Figure 7d), followed by PALSAR + S2 ($R^2 = 0.76$, $RMSE = 26.06$ Mg/ha; Figure 7e). The single data source of S2 still shows the best performance among the three single data sources ($R^2 = 0.72$, $RMSE = 26.90$ Mg/ha; Figure 7b). When comparing the models using the GEDI L4A data as a reference, it was found that similar performance of each data combination was acquired. The best performance was from S1 + S2 ($R^2 = 0.41$, $RMSE = 37.50$ Mg/ha; Figure 7i), next was PALSAR + S2 ($R^2 = 0.41$, $RMSE = 37.57$ Mg/ha; Figure 7j), then it was S2 ($R^2 = 0.37$, $RMSE = 37.23$ Mg/ha; Figure 7d), and the last one was PALSAR ($R^2 = 0.37$, $RMSE = 38.38$ Mg/ha; Figure 7h). The AGB estimation difference between using field measurements and GEDI L4A ranges from 7.88 (S1; Figure 7a,g) to 12.29 Mg/ha (S1 + S2; Figure 7d,i).

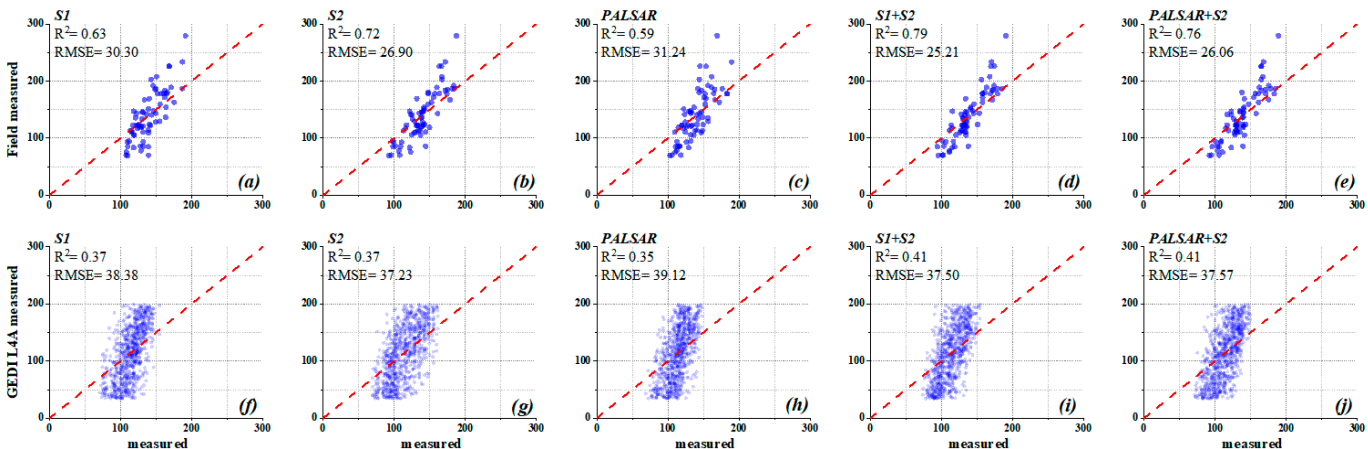


Figure 7. Relationship between measured and predicted AGB values for coniferous forests in the Pu'er study area. The first row subfigures (a–e) uses field measurements as the AGB reference, and the second row subfigures (f–j) uses the GEDI L4A product as the AGB reference. The subfigures (a,f) are for Sentinel-1, the subfigures (b,g) are for Sentinel-2, the subfigures (c,h) are for PALSAR-2, the subfigures (d,i) are for Sentinel-1 and Sentinel-2, and the subfigures (e,j) are for PALSAR-2 and Sentinel-2.

3.3.3. Coniferous Forests in Yiliang

In the AGB estimation of coniferous forests in Yiliang, where the dominated tree species is Yunnan pine (Figure 8), at the sample plot scale, the highest score was the combination of S1 + S2 ($R^2 = 0.84$, RMSE = 7.95 Mg/ha; Figure 8d), followed by PALSAR + S2 ($R^2 = 0.82$, RMSE = 8.32 Mg/ha; Figure 8e). With both the field measurements and GEDI L4A data as AGB reference, using combinations of S1 + S2 and PALSAR + S2 performed better than the performance of single data sources. Among three single data sources, S2 performed best ($R^2 = 0.78$, RMSE = 9.01 Mg/ha; Figure 8b), next was PALSAR ($R^2 = 0.63$, RMSE = 11.14 Mg/ha; Figure 8c), and the last one was S1 ($R^2 = 0.62$, RMSE = 11.30 Mg/ha; Figure 8a). However, compared with other forest types, the estimation difference between using two different references became greater, and ranges from 20.56 (PALSAR; Figure 8c,h) to 23.46 Mg/ha (S1 + S2; Figure 8d,i).

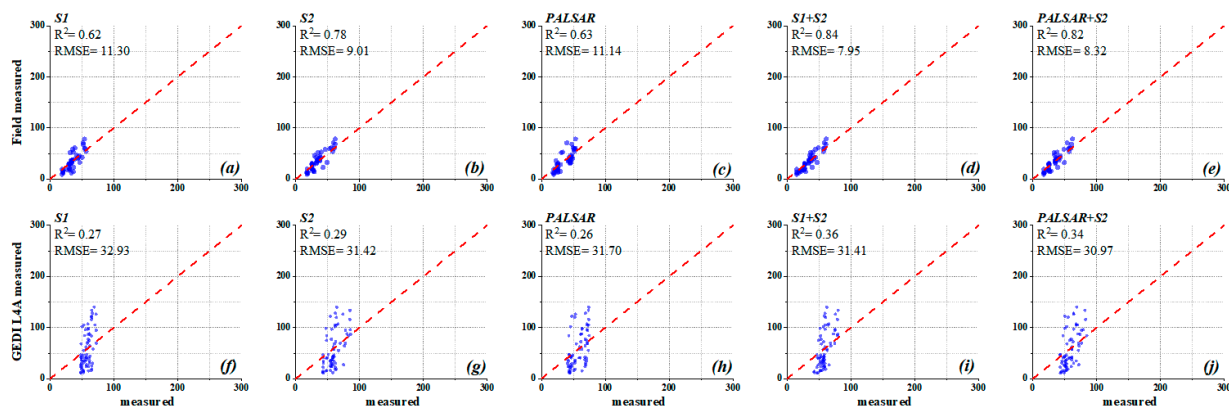


Figure 8. Relationship between measured and predicted AGB values of coniferous forests in the Yiliang study area. The first row subfigures (a–e) uses field measurements as the AGB reference, and the second row subfigures (f–j) uses the GEDI L4A product as the AGB reference. The subfigures (a,f) are for Sentinel-1, the subfigures (b,g) are for Sentinel-2, the subfigures (c,h) are for PALSAR-2, the subfigures (d,i) are for Sentinel-1 and Sentinel-2, and the subfigures (e,j) are for PALSAR-2 and Sentinel-2.

3.4. Forest AGB Mapping and Validation

Based on results from Sections 3.2 and 3.3, the AGB estimation separating forest types performed better. In this section, forest AGB mapping based on three main forest types were generated and validated. The estimates from the AGB maps using GEDI L4A as a reference were validated against the estimates from the AGB maps using the ground sample plot as a reference.

Figure 9 shows the AGB maps and validation results for the broadleaf forest. Figure 9 shows a clear difference between results from the ground sample plot as reference (Figure 9A) and GEDI L4A as reference (Figure 9B). The AGB for the former ranges from 90 to 212 Mg/ha, while the latter ranges from 67 to 170 Mg/ha. The dynamic ranges for both of them are around 100 Mg/ha. It seems that both overestimated AGB with low values and underestimated AGB with high values. The average value of the estimates for the former is 143.81 Mg/ha, which is near 141.68 Mg/ha, and is calculated with an average value of field-collected sample plots. The average value of the estimates for the latter is 127.02 Mg/ha, about 15 Mg/ha lower than 141.68 Mg/ha. The scatter plot (Figure 9C) describes the point-to-point correlations between the two estimated AGB results. The R^2 value between them is 0.50 and the RMSE is 22.40 Mg/ha. The relative error between two estimated AGB is 15.8%.

Figure 10 shows the AGB maps and validation results for coniferous forests in Pu'er. Moreover, Figure 10 demonstrates an obvious difference between results from the ground sample plot as reference (Figure 10A) and GEDI L4A as reference (Figure 10B). Compared with broadleaf forest, the former shows a similar dynamic AGB range with field work (69.61 to 162.30 Mg/ha); however, the overestimation of low AGB is still clear in coniferous AGB estimation using ground sample plot as reference. The average value of the estimates for

the former is 145.17 Mg/ha, which is about 25 Mg/ha higher than 120.89 Mg/ha, calculated with an average value of field-collected sample plots. For the latter, the dynamic range was around 20 Mg/ha narrower than the field-collected results. It seems to underestimate AGB with high AGB values; however, the overestimation level is lower than in the broadleaf forest. Meanwhile, the average value of the estimates for the latter is 113.87 Mg/ha, only around 5 Mg/ha difference with 120.89 Mg/ha. The scatter plot (Figure 10C) describes the point-to-point correlations between the two estimated AGB results with representative areas (A1 and B1). The R^2 value between them is 0.41 and the RMSE is 33.28 Mg/ha. The relative error between two estimated AGB is 26.8%.

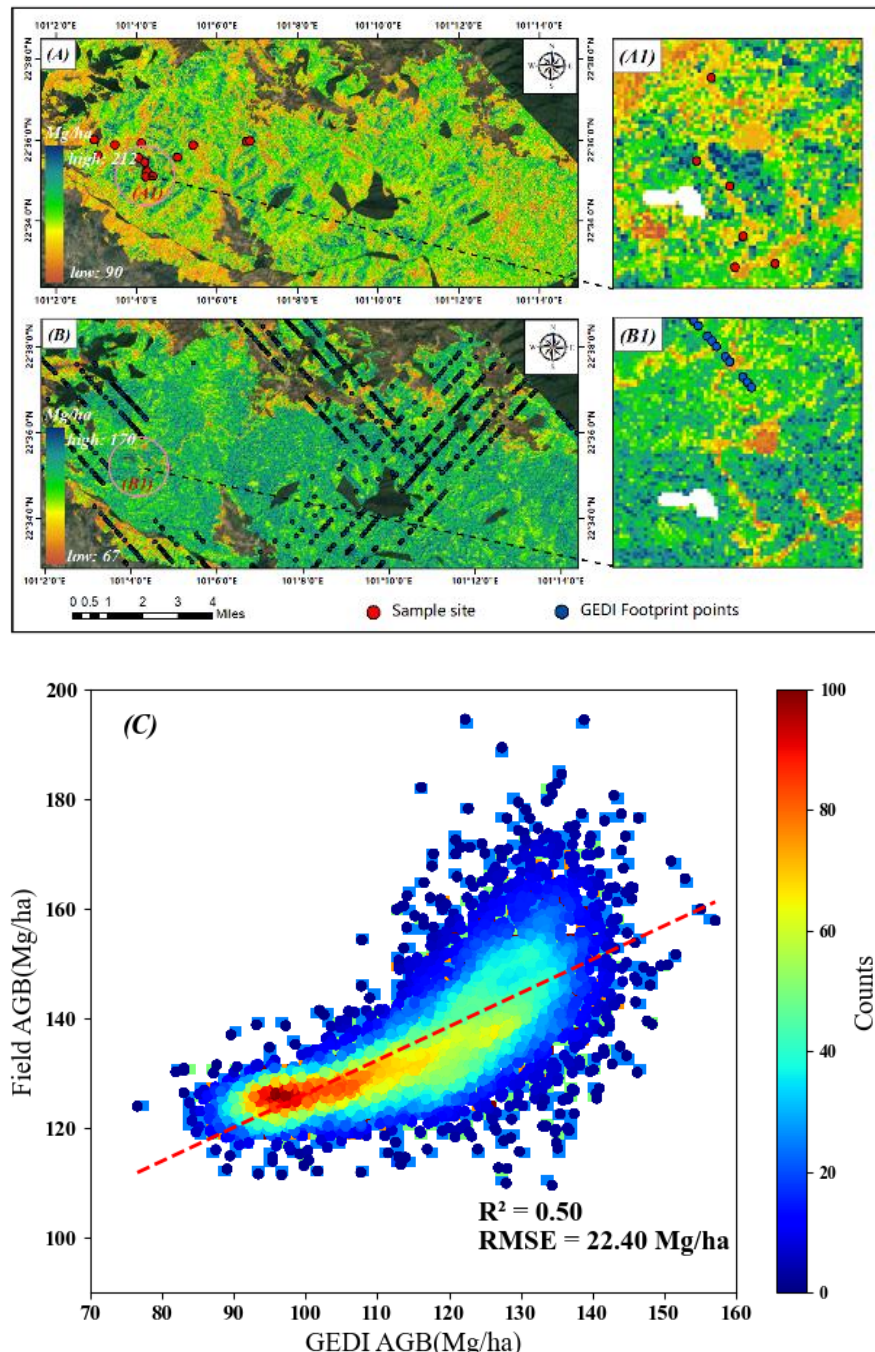


Figure 9. AGB mapping of broadleaf forest. (A) AGB map with the sample plot as reference AGB; (B) AGB map with the GEDI L4A as reference, where (A1) and (B1) represent localized enlargements of the areas corresponding to (A) and (B), respectively. (C) is the scatter plot with comparisons between the inversion values from (A,B). The red dashed line in (C) is the fit line of inversion values from (A,B).

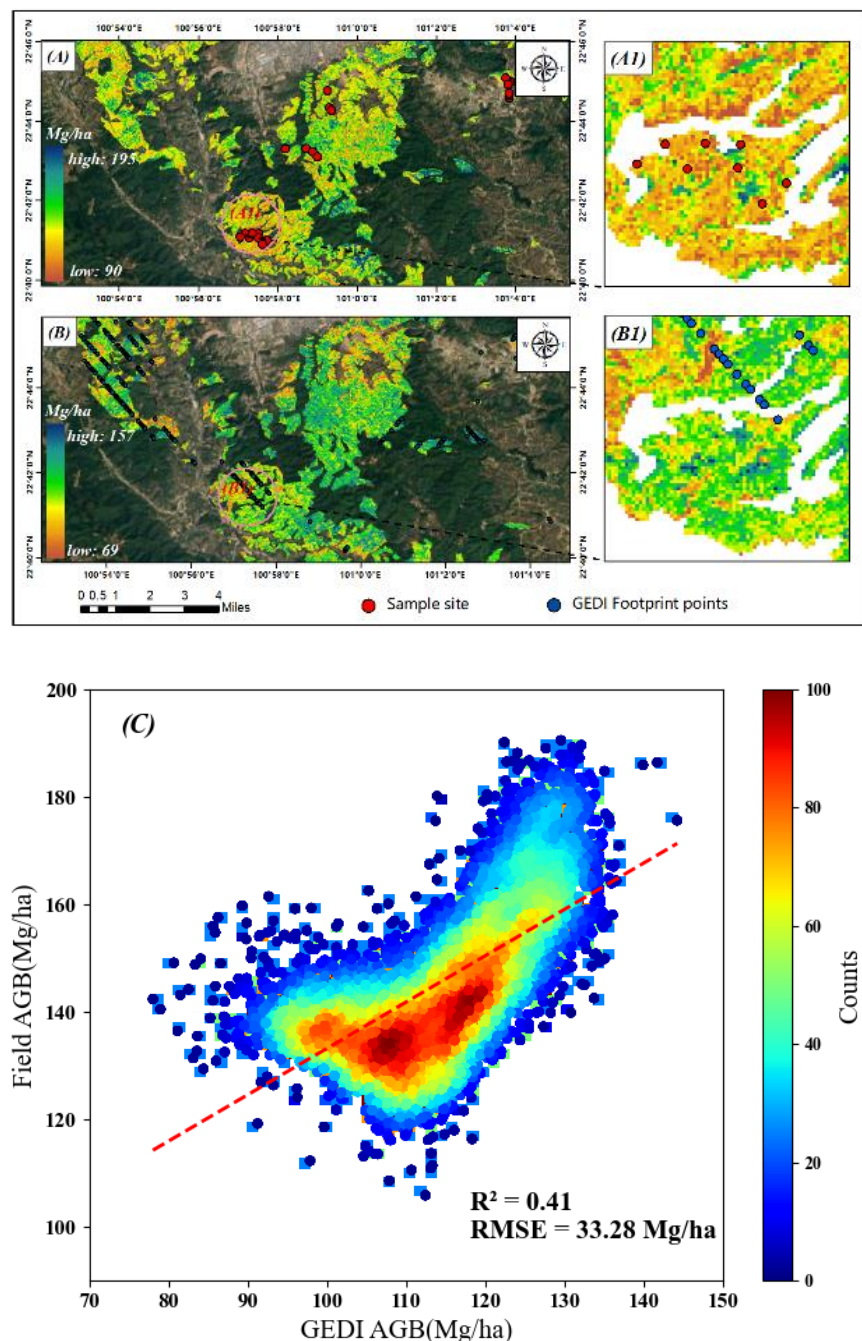


Figure 10. AGB mapping of coniferous forest in Pu'er. (A) AGB map with the sample plot as reference AGB; (B) AGB map with the GEDI L4A as reference, where (A1) and (B1) represent localized enlargements of the areas corresponding to (A) and (B), respectively. (C) is the scatter plot with comparisons between the inversion values from (A,B). The red dashed line in (C) is the fit line of inversion values from (A,B).

Figure 11 illustrates the AGB maps and validation results for coniferous forests in Yiliang. Moreover, Figure 11 reveals the clear narrow dynamic ranges for estimated AGB with ground sample plot as reference (Figure 11A) and GEDI L4A as reference (Figure 11B). The dynamic range for the former is 49 Mg/ha and for the latter is 44 Mg/ha, while the dynamic AGB range from the ground-collected results is from 9.34 to 78.51 Mg/ha. According to Figure 11A, most areas in the map had AGB values from around 20 to 50 Mg/ha, while according to Figure 11B, most areas in the map had AGB values from around 40 to 60 Mg/ha. The density scatter plot (Figure 11C) of the representative area (A1)

and B1) confirmed the high correlation of the two estimates ($R^2 = 0.72$) and the obvious overestimation of using GEDI L4A as a reference with $RMSE = 19.74 \text{ Mg/ha}$. The relative $RMSE$ value between the two estimates increased to 54.6%. Note that the average value of the estimates for the former is 40.32 Mg/ha , for the latter is 59.09 Mg/ha , while the average AGB value field collected in this study area is 36.13 Mg/ha .

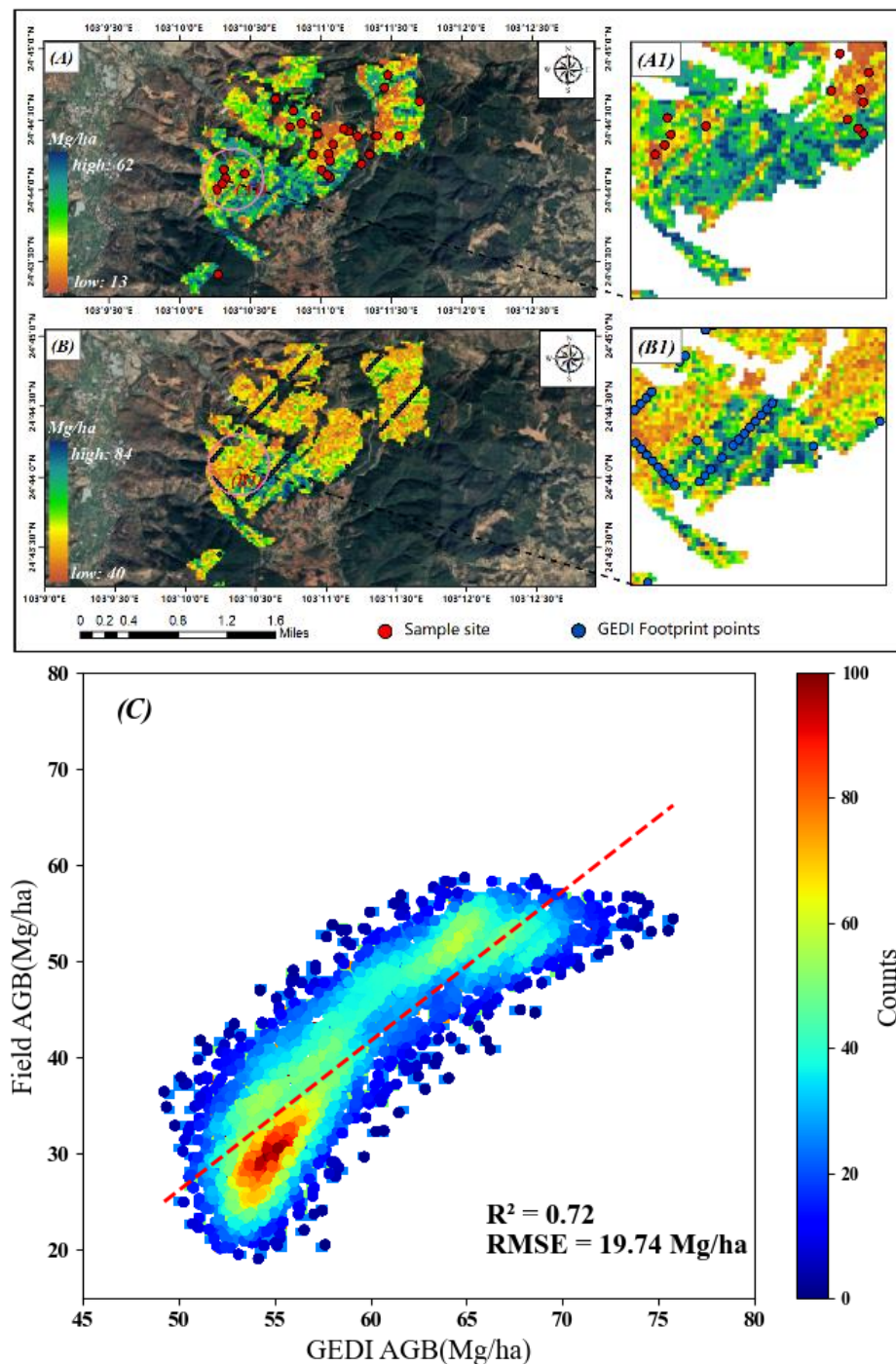


Figure 11. AGB mapping of coniferous forests in Yiliang. (A) AGB map with the sample plot as reference AGB; (B) AGB map with the GEDI L4A as reference, where (A1) and (B1) represent localized enlargements of the areas corresponding to (A) and (B), respectively. (C) is the scatter plot with comparisons between the inversion values from (A,B). The red dashed line in (C) is the fit line of inversion values from (A,B).

3.5. Contribution of Importance of RS Features

The results in Figure 12 demonstrate that the key variables for better performance in different forest AGB estimations are “ARVI”, “NDVI”, and “VV-VH”. Note that there are substantial variations in the importance of these variables when different reference data sources are employed. For example, when referencing GEDI L4A data for AGB, “ARVI” contributes 20.03% and 16.02% in coniferous and broadleaf forests. Meanwhile, certain SAR data features consistently exhibit advantages, such as “VV-VH,” which contribute 6.48% and 21% in the broadleaf forest model. Furthermore, the importance scores for the same variable varied across forest types. For instance, when using GEDI L4A as a reference, “GRVI” contributes 3.78% and 4.49% to broadleaf and coniferous forests, respectively. Vegetation indices related to the red-edge bands, namely, “REIP” and “MTCI”, correspond to the 700–750 nm wavelength range and are linked to chlorophyll content, leaf structure, and biomass; these features show obvious importance in all forest types according to Figure 12. Note that the top three positions of all feature contribution sets include a red-edge vegetation index, albeit with a change in character, i.e., from (a) to (f) REIP, REIP, IRECI, REIP, MTCI, IRECI.

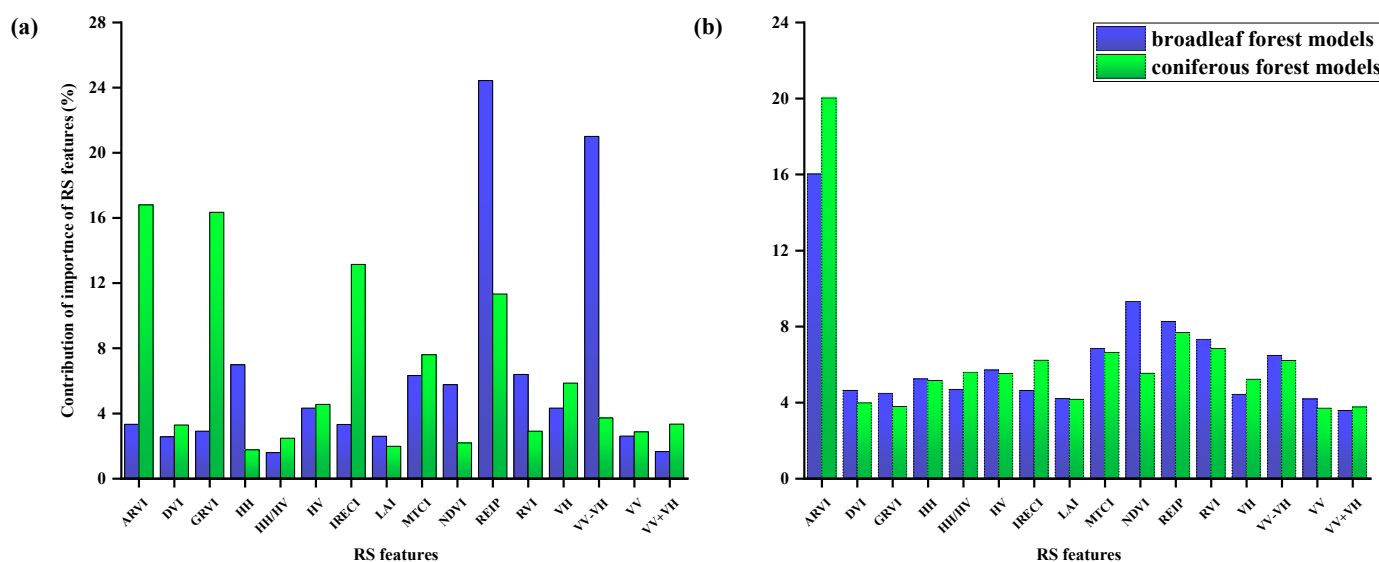


Figure 12. Importance of remote sensing feature contribution in forest AGB estimation, (a) is the rank of remote sensing feature contribution with field as the reference; (b) is the rank of remote sensing feature contribution with GEDI L4A as the reference.

3.6. Empirical Distribution Functions of Field, GEDI, and Predicted AGB

Figure 13 displays plots of empirical distribution functions and histograms of frequency distributions for the broadleaf forest model based on field and GEDI data. The mean value for field AGB is 137.70 Mg/ha, and the predicted AGB mean is 137.37 Mg/ha. Meanwhile, GEDI AGB has a mean of 125.54 Mg/ha, with the predicted AGB mean at 125.06 Mg/ha. Regarding frequency distribution, both field AGB and predicted AGB exhibit similar frequency distributions (Figure 13b), concentrated in the range of 100–180 Mg/ha. Conversely, the frequencies based on GEDI AGB are predominantly in the range of 80–170 Mg/ha (Figure 13d). The K-S statistic measures the maximum vertical distance between the empirical distribution functions, indicating the magnitude of the difference in distribution between them. The smaller the K-S value, the smaller the difference, and vice versa. From the empirical distribution function perspective, the distributions of field AGB and field predicted AGB (Figure 13a) are similar ($K-S = 0.14$). In contrast, the distributions of GEDI and GEDI predicted AGB (Figure 13a) are significantly different ($K-S = 0.28$). The differences in field predictions are smaller compared to GEDI AGB predictions.

Figure 14 displays the empirical distribution function plots and frequency distribution histograms of the coniferous forest models based on field and GEDI data. The mean value of field AGB is 109.96 Mg/ha, while the mean value of predicted AGB from the field data is 109.72 Mg/ha. Similarly, the mean value of GEDI AGB is 101.50 Mg/ha, and the mean value of predicted AGB from GEDI data is 100.58 Mg/ha. It is observed that the mean values of both field AGB and field predicted AGB are similar, as are the mean values of GEDI AGB and GEDI predicted AGB. From the frequency distribution histograms, it is evident that the distribution of field AGB is more uniform (Figure 14b), whereas the distribution of GEDI AGB is predominantly concentrated in the range of 50–150 Mg/ha (Figure 14d). The K-S value between field AGB and field predicted AGB is 0.14 (Figure 14a), indicating a small difference in distribution between them. Conversely, the K-S value for GEDI AGB and GEDI predicted AGB is 0.27 (Figure 14c), suggesting a larger distributional difference between them. Compared to broadleaf forests, the differences in GEDI and field AGB predictions based on coniferous forests are smaller.

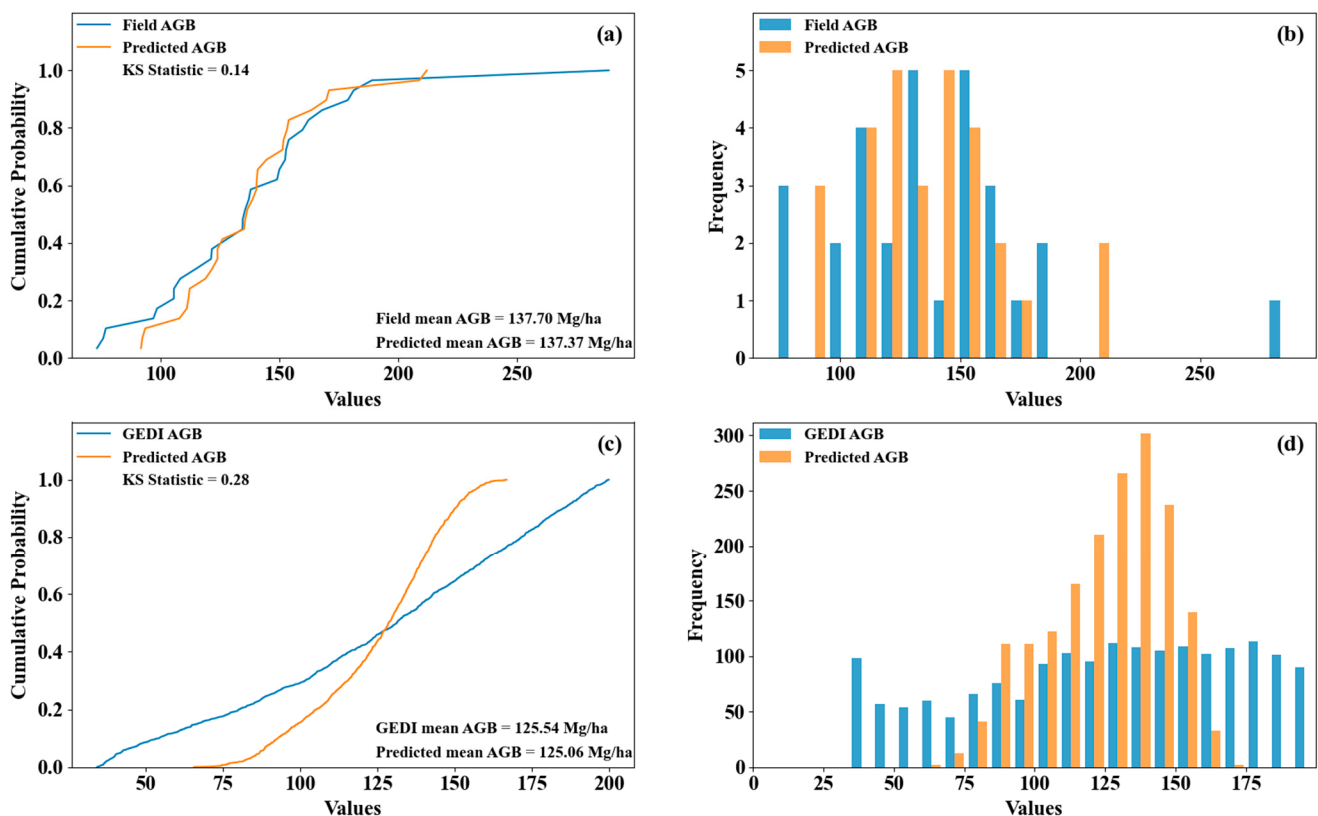


Figure 13. (a) Plot of empirical distribution function of field AGB for broadleaf forests; (b) frequency histogram of field AGB; (c) plot of empirical distribution function of GEDI AGB; (d) frequency histogram of GEDI AGB.

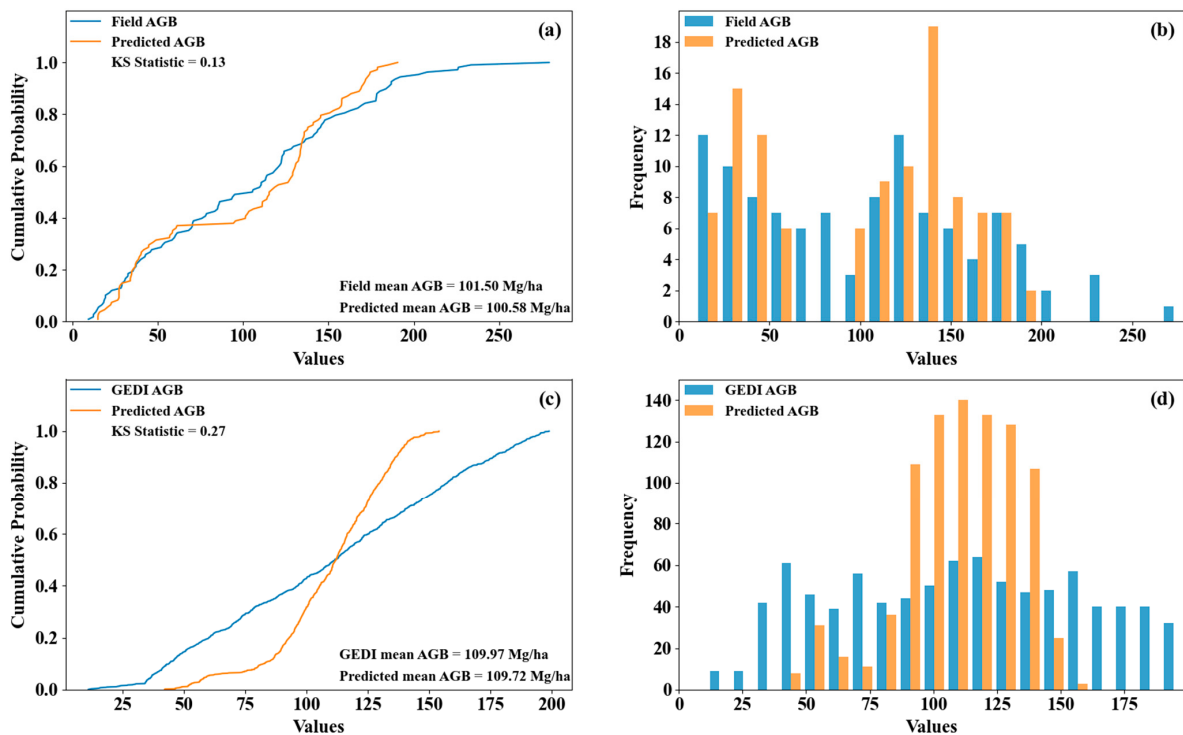


Figure 14. (a) Plot of empirical distribution function of field AGB for coniferous forests; (b) frequency histogram of field AGB; (c) plot of empirical distribution function of GEDI AGB; (d) frequency histogram of GEDI AGB.

4. Discussion

In this study, single-source remote sensing datasets Sentinel-1, Sentinel-2, and ALOS PALSAR-2 and multi-source remote sensing datasets combining Sentinel-1 + Sentinel-2 and ALOS PALSAR-2 + Sentinel-2 were used for regional forest AGB estimation and mapping. An optimal regression algorithm was selected based on the performance comparison of four traditional linear and machine learning models. GEDI AGB products and field-collected ground sample plots were selected and compared as reference AGB values for forest AGB estimates and mapping within different forest types.

RF performed better than KNN, GBRT, and linear regression in forest AGB estimation and was applied for forest AGB estimation and mapping within three different forest types. RF outperforms most parametric and nonparametric models in forest AGB estimation. Its best performance was confirmed by several previous studies for forest AGB estimation [40,41]. RF has strong predictive power for more complex datasets [42]. RF has been shown to be a suitable modeling technique for estimating forest AGB using hyperspectral and LiDAR data and combinations of hyperspectral and LiDAR data [19,43,44]. For the remote sensing data sources, combinations of optical and SAR data showed better performance than single optical and single SAR datasets [41,45–47]. The combination of S1 + S2 and PALSAR + S2 performed almost the same in the results both using ground sample plot as reference and GEDI L4A as reference. Among single remote sensing data sources, optical data S2 performed better than SAR data of S1 and PALSAR. According to previous studies [40,41,48,49], the better performance of the optical data in forest AGB estimation may result from the good response of integration of optical textures and spectral features to low forest AGB level (average AGB lower than 150 Mg/ha). The results revealed that in forest areas with lower AGB, optical features show higher accurate estimation than SAR data. The advantages of high penetration of C- or L-band in the forest do not necessarily result in better performance of SAR, when it comes to forest AGB retrieval using machine learning for these test sites. It has been shown that there is a strong positive correlation between forest biomass and vegetation index, and the potential of vegetation index in forest biomass estimation has been

demonstrated [50]. Meanwhile, combining SAR factors is particularly important in estimating forest biomass [51]. In this study, the combination of S2 + S1 performed better than the S2 + PALSAR, the phenomenon may result from the forest vertical structures in the test sites. In the test sites, the average forest AGB is low and the trees are young with low forest height, since C-band has a lower wavelength than L-band, and more scattering from trunk-like double-bounce scattering reflected than that in L-band. It may result in the better performance of C-band than L-band. Moreover, it is possible that the difference in inversion modeling may result in C-band, which would have better correlation with forest AGB [52]. It is worth noting that the accuracy of AGB estimation can be improved when remote sensing factors contain red-edge bands, such as vegetation indices like “IRECI” and “MTCI”, probably because the red-edge information is related to canopy thickness and leaf area. Horler et al. and Vaglio et al. had demonstrated the correlation between red-edge information and AGB prediction in their studies [53,54].

The AGB estimations using GEDI L4A as a reference underperformed compared to using ground sample plots as a reference. The results were in line with the work of Kanmegne et al. conducted in West Africa for forest AGB estimation in agroforestry [41]. The difference between them was affected by forest types. In this study, the RMSE values between the estimates obtained with the ground sample plot and GEDI L4A as reference are from around 10 to 23.46 Mg/ha, and the relative RMSE ranges from 16.2% to 64.9%. In the AGB mapping results, the estimation difference between them ranges from 15.8% to 52.6%. The performance differs between different forest types or the same forest type but with different dominated tree species. The differences were lower in broadleaf forests (15.8%) and coniferous forests in Pu'er (26.8%), while a greater difference was shown in coniferous forests in Yiliang (52.6%). In terms of distributional empirical functions, the K-S statistic for GEDI in coniferous forests was significantly larger than that for field AGB, and the variability in sample site estimates was relatively small. The worse performance of using GEDI L4A as a reference may result from the distribution of the GEDI L4A samples which cannot show the representative of the forest AGB level in the study areas. For the higher difference in coniferous forests in Yiliang, it may result from the complicated terrain and shortage of enough GEDI L4A samples in the study area [55,56], this may lead to a reduction in the training samples for the model, as well as the lack of the principle of spatial random distribution of the light patches of GEDI. Second, GEDI signals can be distorted by topographic conditions within their footprint, leading to uncertainty in estimated forest AGB. The accuracy of AGB estimation was improved when the slope was $<10^\circ$ [57], and a significant improvement in the accuracy of AGB estimation was observed when the slope was in the range of 0–40° with a decrease in RMSE of 20.83 Mg/ha [58]. Ref. [41] demonstrated the effect of vegetation type on forest AGB estimates. It demonstrated that the RMSE values acquired using GEDI L4A samples as reference were found to be 8.94 times higher than those using the ground sample plot as a reference. Previous studies in forest AGB inversion also stated that distinguishing forest types and AGB levels had a significant impact on AGB estimation performance [40,59,60]. Stratified approaches based on forest type and AGB range may have great potential for improving AGB estimation if an adequate number of sample plots is available [40,41,61].

From 2013 to 2021, China's forest aboveground biomass products [62] (dataset No. f48c4983dbd84a4c9c287111ac91c5aa) were published by the China Science Data Center, covering forest AGB data at a 30 m resolution for China's land areas. In this study, the 2021 forest AGB map of Yunnan Province was used for spatial analysis to verify the accuracy of the forest AGB prediction maps in the two study areas of Yiliang and Pu'er. The product map of forest AGB in China in 2021 is illustrated in Figure 15a,d. Visual interpretation revealed that the spatial distribution of AGB in this product showed a similar pattern to the predicted AGB map in this study. In the Yiliang study area (Figure 15b), the predicted AGB of forests in the sample plots is mainly distributed between 20 and 60 Mg/ha, whereas forest AGB based on GEDI inversion showed the largest proportion of pixels with AGB values between 45 and 75 Mg/ha (Figure 15c). This is similar to the range

of China forest AGB products in the Yiliang area, which are mostly distributed between 45 and 85 Mg/ha (Figure 15a). The forest AGB of the field survey in Yiliang area ranged from 9.34–78.51 Mg/ha, and the range of forest AGB based on GEDI and field plots data inversion is close to this range. In the Pu'er study area, China forest AGB products are mainly distributed between 70 and 220 Mg/ha (Figure 15d), which is consistent with the predicted forest AGB map based on field plots data and showed high values close to each other. In addition, the predicted distribution of forest AGB based on GEDI is close to that of China forest AGB products, showing an increasing trend from north to south in the study area, and the distribution is relatively uniform, with AGB values mainly concentrated around 75 Mg/ha. The high values in the above three types of forest AGB data are all within the range of AGB (69.61–288.68 Mg/ha) of the field survey in Pu'er, and the predicted low values of AGB in the GEDI are close to the values of AGB of the field survey in Pu'er.

GEDI is the significant climatic project from NASA with the objective of improving our knowledge of the function of forests in global carbon cycle. It delivers forest canopy height and forest AGB products in global scale. To further validate the accuracy and capability of these products for calculating accurate forest carbon storage is necessary and important for the goal of achieving the neutrality of greenhouse gas emission in future. In this study, we compared the forest AGB estimation difference that resulted from using GEDI L4A AGB samples and ground sample plots as true AGB values, respectively. The results revealed the potential of using GEDI L4A AGB samples as a true AGB value for forest AGB estimation using different remote sensing datasets. However, only several forest types were involved in this study, the potability and suitability of GEDI L4A AGB samples working as a true value in other forest types need to further explored.

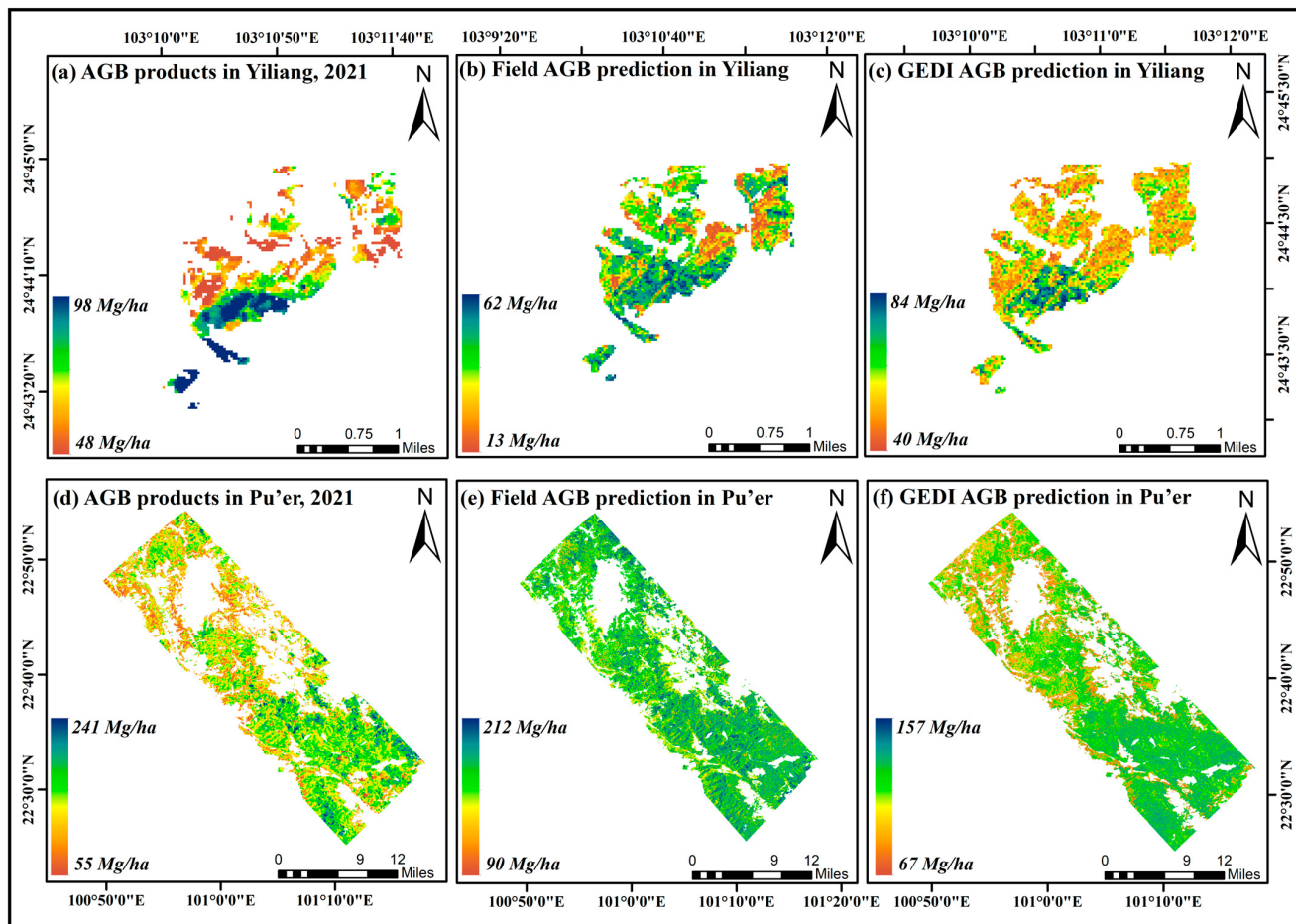


Figure 15. Comparison maps of AGB products of forests in Yiliang and Pu'er study areas with those in China. (a,d) Represent maps of AGB products in Yiliang and Pu'er in 2021, respectively;

(b,c) represent maps of AGB projections of forests in the Yiliang study area based on sample plots and GEDI, respectively; and (e,f) represent maps of AGB projections in the Pu'er study area based on sample plots and GEDI, respectively.

5. Conclusions

This study systematically investigated the AGB inversion of special forest types in Yunnan Province using single optical, SAR, and multi-sources remote sensing datasets like the combination of optical and C-band SAR and the combination of optical and L-band SAR datasets. We explored ground sample plots and GEDI L4A as reference and used an RF algorithm for forest AGB estimation. Their performance was compared to show the capability of substituting GEDI L4A for ground sample plots and the influence of forest types. (1) We found in the forest area with low AGB (lower than 150 Mg/ha) that the combination of optical and SAR data shows better performance than single optical or SAR datasets. (2) Among the four selected inversion algorithms, RF performed best in forest AGB estimation. (3) The AGB predictions from the GEDI L4A AGB product used as a reference underperformed compared to the ground sample plots used as a reference. The differences between them are lower in broadleaf forests and coniferous forests dominated by Simao pine, while they are high in coniferous forests dominated by *Yunnan pine*. Using red-edge bands of optical data show clear improvement for the AGB estimation. In summary, GEDI can work as ground truth data source for forest AGB estimation in a certain level of estimation accuracy. Note that, in this study, only ground sample plots as reference were compared with GEDI L4A AGB product as reference, they were not compared with the airborne LiDAR-derived AGB products since these datasets are not available. Moreover, the distribution and density of the ground sample plot and GEDI L4A footprints may affect the estimated AGB results, and need to be further explored in our future studies.

Author Contributions: Conceptualization, Y.J.; methodology, C.W.; project administration, W.Z. and Y.J.; resources, C.L., Y.J. and W.Z.; software, M.W., L.W., C.W. and H.Z.; supervision, Y.J. and W.Z.; validation, C.W. and M.W.; writing—original draft preparation, C.W. and W.Z.; writing—review and editing, W.Z., A.M., C.L. and Y.J.; visualization, C.W. and H.Z. All authors have read and agreed to the published version of the manuscript.

Funding: This research was funded by the National Natural Science Foundation of China, grant numbers 32160365, 42161059, 32371869, and 31860240 and the Agriculture Joint Special Project of Yunnan Province, grant number 202301BD070001-058.

Data Availability Statement: Sentinel-1, Sentinel-2, and ALOS data are available for downloading through the GEE platform (<https://earthengine.google.com/>, accessed on 22 September 2023) and GEDI (<https://search.earthdata.nasa.gov/>, accessed on 23 September 2023). Forest aboveground biomass products in China (<https://www.scidb.cn/en/detail?dataSetId=f48c4983dbd84a4c9c287111ac91c5aa&dataSetType=journal&code=j00001&tID=journalOne>, accessed on 9 October 2023). Field-collected data are available and can be obtained by contacting the corresponding author.

Acknowledgments: The authors would like to thank everyone who helped to improve the quality of the manuscripts.

Conflicts of Interest: Chunmei Li was employed by China Spacesat Co., Ltd. The remaining authors declare that the research was conducted in the absence of any commercial or financial relationships that could be construed as a potential conflict of interest. The China Spacesat Co., Ltd. had no role in the design of the study; in the collection, analyses, or interpretation of data; in the writing of the manuscript, or in the decision to publish the results.

References

1. Yang, J. Estimation of Forest Ecological and Social Benefits Based on Forest Inventory. *Mod. Gard.* **2022**, *45*, 186–188. [[CrossRef](#)]
2. Wang, X. Importance of Forest Resource Conservation and Management and Analysis of Strategies. *Shanxi For. Sci. Technol.* **2023**, *52*, 61–62. [[CrossRef](#)]

3. Fang, J.; Wang, G.G.; Liu, G.; Xu, S. Forest Biomass of China: An Estimate Based on the Biomass–Volume Relationship. *Ecol. Appl.* **1998**, *8*, 1084–1091. [[CrossRef](#)]
4. Bolin, B. Changes of Land Biota and Their Importance for the Carbon Cycle. *Science* **1977**, *196*, 613–615. [[CrossRef](#)] [[PubMed](#)]
5. Brown, S.; Lugo, A.E. Biomass of Tropical Forests: A New Estimate Based on Forest Volumes. *Science* **1984**, *223*, 1290–1293. [[CrossRef](#)]
6. Brown, S.; Lugo, A.E. The Storage and Production of Organic Matter in Tropical Forests and Their Role in the Global Carbon Cycle. *Biotropica* **1982**, *14*, 161–187. [[CrossRef](#)]
7. Potapov, P.; Li, X.; Hernandez-Serna, A.; Tyukavina, A.; Hansen, M.C.; Kommareddy, A.; Pickens, A.; Turubanova, S.; Tang, H.; Silva, C.E.; et al. Mapping Global Forest Canopy Height through Integration of GEDI and Landsat Data. *Remote Sens. Environ.* **2021**, *253*, 112165. [[CrossRef](#)]
8. Botequim, B.; Fernandes, P.M.; Borges, J.G.; González-Ferreiro, E.; Guerra-Hernández, J.; Botequim, B.; Fernandes, P.M.; Borges, J.G.; González-Ferreiro, E.; Guerra-Hernández, J. Improving Silvicultural Practices for Mediterranean Forests through Fire Behaviour Modelling Using LiDAR-Derived Canopy Fuel Characteristics. *Int. J. Wildland Fire* **2019**, *28*, 823–839. [[CrossRef](#)]
9. Narine, L.L.; Popescu, S.C.; Malambo, L. Synergy of ICESat-2 and Landsat for Mapping Forest Aboveground Biomass with Deep Learning. *Remote Sens.* **2019**, *11*, 1503. [[CrossRef](#)]
10. Dobson, M.C.; Ulaby, F.T.; LeToan, T.; Beaudoin, A.; Kasischke, E.S.; Christensen, N. Dependence of Radar Backscatter on Coniferous Forest Biomass. *IEEE Trans. Geosci. Remote Sens.* **1992**, *30*, 412–415. [[CrossRef](#)]
11. Lin, J.; Chen, D.; Wu, W.; Liao, X. Estimating Aboveground Biomass of Urban Forest Trees with Dual-Source UAV Acquired Point Clouds. *Urban For. Urban Green.* **2022**, *69*, 127521. [[CrossRef](#)]
12. Li, L.; Zhou, X.; Chen, L.; Chen, L.; Zhang, Y.; Liu, Y. Estimating Urban Vegetation Biomass from Sentinel-2A Image Data. *Forests* **2020**, *11*, 125. [[CrossRef](#)]
13. Askar, U.; Nuthammachot, N.; Phairuang, W.; Wicaksono, P.; Sayektinginsih, T. Estimating Aboveground Biomass on Private Forest Using Sentinel-2 Imagery. *J. Sens.* **2018**, *2018*, e6745629. [[CrossRef](#)]
14. Han, H.; Wan, R.; Li, B. Estimating Forest Aboveground Biomass Using Gaofen-1 Images, Sentinel-1 Images, and Machine Learning Algorithms: A Case Study of the Dabie Mountain Region, China. *Remote Sens.* **2022**, *14*, 176. [[CrossRef](#)]
15. Delegido, J.; Verrelst, J.; Alonso, L.; Moreno, J. Evaluation of Sentinel-2 Red-Edge Bands for Empirical Estimation of Green LAI and Chlorophyll Content. *Sensors* **2011**, *11*, 7063–7081. [[CrossRef](#)]
16. Forkuor, G.; Benewinde Zoungrana, J.-B.; Dimobe, K.; Ouattara, B.; Vadrevu, K.P.; Tondoh, J.E. Above-Ground Biomass Mapping in West African Dryland Forest Using Sentinel-1 and 2 Datasets—A Case Study. *Remote Sens. Environ.* **2020**, *236*, 111496. [[CrossRef](#)]
17. Nuthammachot, N.; Askar, A.; Stratoulias, D.; Wicaksono, P. Combined Use of Sentinel-1 and Sentinel-2 Data for Improving above-Ground Biomass Estimation. *Geocarto Int.* **2022**, *37*, 366–376. [[CrossRef](#)]
18. Zhang, L.; Zhang, X.; Shao, Z.; Jiang, W.; Gao, H. Integrating Sentinel-1 and 2 with LiDAR Data to Estimate Aboveground Biomass of Subtropical Forests in Northeast Guangdong, China. *Int. J. Digit. Earth* **2023**, *16*, 158–182. [[CrossRef](#)]
19. Shao, Z.; Zhang, L. Estimating Forest Aboveground Biomass by Combining Optical and SAR Data: A Case Study in Genhe, Inner Mongolia, China. *Sensors* **2016**, *16*, 834. [[CrossRef](#)]
20. Liu, W.; Xu, C.; Zhang, Z.; De Boeck, H.; Wang, Y.; Zhang, L.; Xu, X.; Zhang, C.; Chen, G.; Xu, C. Machine Learning-Based Grassland Aboveground Biomass Estimation and Its Response to Climate Variation in Southwest China. *Front. Ecol. Evol.* **2023**, *11*, 1146850. [[CrossRef](#)]
21. Tu, H.; Ma, G.; Pan, Z.; Li, H.; Zhang, R.; Yao, X. Assessment of Forest Ecosystem Service Function Value in Yunnan Province. *Guangxi For. Sci.* **2023**, *52*, 23–30. [[CrossRef](#)]
22. Peng, J.; Zhu, K.; Xu, H.; Huang, X.; Dai, J.; Huang, R. Exploring the Development of Highland Mountain Forest Cities in Yunnan Province. *For. Resour. Manag.* **2021**, 23–29. [[CrossRef](#)]
23. Hu, Z. Analysis and Evaluation of Dynamic Changes of Forest Resources in Yunnan Province. *For. Surv. Plan.* **2017**, *42*, 87–94+99.
24. Meng, X. *Forest Mensuration*; China Forestry Publishing House: Beijing, China, 2006.
25. Luo, Y.; Wang, X.; Lu, F. *Comprehensive Database of Biomass Regressions for China's Tree Species*; China Forestry Publishing House: Beijing, China, 2015.
26. Xu, H.; Zhang, H. *Forest Tree Biomass Modeling*; Yunnan Science and Technology Press: Kunming, China, 2002.
27. Shimada, M.; Itoh, T.; Motooka, T.; Watanabe, M.; Shiraishi, T.; Thapa, R.; Lucas, R. New Global Forest/Non-Forest Maps from ALOS PALSAR Data (2007–2010). *Remote Sens. Environ.* **2014**, *155*, 13–31. [[CrossRef](#)]
28. Xue, J.; Su, B. Significant Remote Sensing Vegetation Indices: A Review of Developments and Applications. *J. Sens.* **2017**, *2017*, e1353691. [[CrossRef](#)]
29. Xi, Z.; Xu, H.; Xing, Y.; Gong, W.; Chen, G.; Yang, S. Forest Canopy Height Mapping by Synergizing ICESat-2, Sentinel-1, Sentinel-2 and Topographic Information Based on Machine Learning Methods. *Remote Sens.* **2022**, *14*, 364. [[CrossRef](#)]
30. Bhattacharai, R.; Rahimzadeh-Bajgiran, P.; Weiskittel, A.; MacLean, D.A. Sentinel-2 Based Prediction of Spruce Budworm Defoliation Using Red-Edge Spectral Vegetation Indices. *Remote Sens. Lett.* **2020**, *11*, 777–786. [[CrossRef](#)]
31. Vesanto, V.-H.; Möttus, M.; Heiskanen, J.; Rautiainen, M.; Majasalmi, T. Atmospheric Correction of a Seasonal Time Series of Hyperion EO-1 Images and Red Edge Inflection Point Calculation. In Proceedings of the 2012 4th Workshop on Hyperspectral Image and Signal Processing: Evolution in Remote Sensing (WHISPERS), Shanghai, China, 4–7 June 2012; pp. 1–4.

32. Puliti, S.; Breidenbach, J.; Schumacher, J.; Hauglin, M.; Klingenberg, T.F.; Astrup, R. Above-Ground Biomass Change Estimation Using National Forest Inventory Data with Sentinel-2 and Landsat. *Remote Sens. Environ.* **2021**, *265*, 112644. [[CrossRef](#)]
33. Kellner, J.R.; Armston, J.; Duncanson, L. Algorithm Theoretical Basis Document for GEDI Footprint Aboveground Biomass Density. *Earth Space Sci.* **2023**, *10*, e2022EA002516. [[CrossRef](#)]
34. Shams, M.Y.; Elshewey, A.M.; El-kenawy, E.-S.M.; Ibrahim, A.; Talaat, F.M.; Tarek, Z. Water Quality Prediction Using Machine Learning Models Based on Grid Search Method. In *Multimedia Tools and Applications*; Springer: Berlin/Heidelberg, Germany, 2023. [[CrossRef](#)]
35. Zhang, Y.; Ma, J.; Liang, S.; Li, X.; Li, M. An Evaluation of Eight Machine Learning Regression Algorithms for Forest Aboveground Biomass Estimation from Multiple Satellite Data Products. *Remote Sens.* **2020**, *12*, 4015. [[CrossRef](#)]
36. Jiang, F.; Sun, H.; Ma, K.; Fu, L.; Tang, J. Improving Aboveground Biomass Estimation of Natural Forests on the Tibetan Plateau Using Spaceborne LiDAR and Machine Learning Algorithms. *Ecol. Indic.* **2022**, *143*, 109365. [[CrossRef](#)]
37. Moradi, F.; Darvishsefat, A.A.; Pourrahmati, M.R.; Deljouei, A.; Borz, S.A. Estimating Aboveground Biomass in Dense Hyrcanian Forests by the Use of Sentinel-2 Data. *Forests* **2022**, *13*, 104. [[CrossRef](#)]
38. McRoberts, R.E.; Tomppo, E.O. Remote Sensing Support for National Forest Inventories. *Remote Sens. Environ.* **2007**, *110*, 412–419. [[CrossRef](#)]
39. Shataee, S.; Kalbi, S.; Fallah, A.; Pelz, D. Forest Attribute Imputation Using Machine-Learning Methods and ASTER Data: Comparison of k-NN, SVR and Random Forest Regression Algorithms. *Int. J. Remote Sens.* **2012**, *33*, 6254–6280. [[CrossRef](#)]
40. Gao, Y.; Lu, D.; Li, G.; Wang, G.; Chen, Q.; Liu, L.; Li, D. Comparative Analysis of Modeling Algorithms for Forest Aboveground Biomass Estimation in a Subtropical Region. *Remote Sens.* **2018**, *10*, 627. [[CrossRef](#)]
41. Kanmegne Tamga, D.; Latifi, H.; Ullmann, T.; Baumhauer, R.; Bayala, J.; Thiel, M. Estimation of Aboveground Biomass in Agroforestry Systems over Three Climatic Regions in West Africa Using Sentinel-1, Sentinel-2, ALOS, and GEDI Data. *Sensors* **2023**, *23*, 349. [[CrossRef](#)]
42. Pal, M. Random Forest Classifier for Remote Sensing Classification. *Int. J. Remote Sens.* **2005**, *26*, 217–222. [[CrossRef](#)]
43. Fassnacht, F.E.; Hartig, F.; Latifi, H.; Berger, C.; Hernández, J.; Corvalán, P.; Koch, B. Importance of Sample Size, Data Type and Prediction Method for Remote Sensing-Based Estimations of Aboveground Forest Biomass. *Remote Sens. Environ.* **2014**, *154*, 102–114. [[CrossRef](#)]
44. Latifi, H.; Nothdurft, A.; Koch, B. Non-Parametric Prediction and Mapping of Standing Timber Volume and Biomass in a Temperate Forest: Application of Multiple Optical/LiDAR-Derived Predictors. *For. Int. J. For. Res.* **2010**, *83*, 395–407. [[CrossRef](#)]
45. Silva, C.A.; Duncanson, L.; Hancock, S.; Neuenschwander, A.; Thomas, N.; Hofton, M.; Fatoyinbo, L.; Simard, M.; Marshak, C.Z.; Armston, J.; et al. Fusing Simulated GEDI, ICESat-2 and NISAR Data for Regional Aboveground Biomass Mapping. *Remote Sens. Environ.* **2021**, *253*, 112234. [[CrossRef](#)]
46. Campbell, M.J.; Dennison, P.E.; Kerr, K.L.; Brewer, S.C.; Anderegg, W.R.L. Scaled Biomass Estimation in Woodland Ecosystems: Testing the Individual and Combined Capacities of Satellite Multispectral and Lidar Data. *Remote Sens. Environ.* **2021**, *262*, 112511. [[CrossRef](#)]
47. Shendryk, Y. Fusing GEDI with Earth Observation Data for Large Area Aboveground Biomass Mapping. *Int. J. Appl. Earth Obs. Geoinf.* **2022**, *115*, 103108. [[CrossRef](#)]
48. Lu, D.; Chen, Q.; Wang, G.; Liu, L.; Li, G.; Moran, E. A Survey of Remote Sensing-Based Aboveground Biomass Estimation Methods in Forest Ecosystems. *Int. J. Digit. Earth* **2016**, *9*, 63–105. [[CrossRef](#)]
49. Lone, J.M.; Sivasankar, T.; Pebam, R.; Sarma, K.K.; Qadir, M.A.; Raju, P.L.N. Comparison of C-Band Sentinel-1 and L-Band ALOSPALSAR-2 Data for Aboveground Forest Biomass Estimation over Nongkhylliem Forest Reserve and Wildlife Sanctuary, Meghalaya, India. In Proceedings of the Advances in Remote Sensing & GIS Applications, North Eastern Space Applications Centre, Umiam, Meghalaya, India, 10–11 May 2018.
50. Pandit, S.; Tsuyuki, S.; Dube, T. Estimating Above-Ground Biomass in Sub-Tropical Buffer Zone Community Forests, Nepal, Using Sentinel 2 Data. *Remote Sens.* **2018**, *10*, 601. [[CrossRef](#)]
51. Laurin, G.V.; Balling, J.; Corona, P.; Mattioli, W.; Papale, D.; Puletti, N.; Rizzo, M.; Truckenbrodt, J.; Urban, M. Above-Ground Biomass Prediction by Sentinel-1 Multitemporal Data in Central Italy with Integration of ALOS2 and Sentinel-2 Data. *J. Appl. Remote Sens.* **2018**, *12*, 016008. [[CrossRef](#)]
52. Zeng, P.; Zhang, W.; Li, Y.; Shi, J.; Wang, Z. Forest Total and Component Above-Ground Biomass (AGB) Estimation through C- and L-Band Polarimetric SAR Data. *Forests* **2022**, *13*, 442. [[CrossRef](#)]
53. Horler, D.N.H.; Dockray, M.; Barber, J.; Barringer, A.R. Red Edge Measurements for Remotely Sensing Plant Chlorophyll Content. *Adv. Space Res.* **1983**, *3*, 273–277. [[CrossRef](#)]
54. Vaglio Laurin, G.; Chen, Q.; Lindsell, J.A.; Coomes, D.A.; Frate, F.D.; Guerriero, L.; Pirotti, F.; Valentini, R. Above Ground Biomass Estimation in an African Tropical Forest with Lidar and Hyperspectral Data. *ISPRS J. Photogramm. Remote Sens.* **2014**, *89*, 49–58. [[CrossRef](#)]
55. Araza, A.; de Bruin, S.; Herold, M.; Quegan, S.; Labriere, N.; Rodriguez-Veiga, P.; Avitabile, V.; Santoro, M.; Mitchard, E.T.A.; Ryan, C.M.; et al. A Comprehensive Framework for Assessing the Accuracy and Uncertainty of Global Above-Ground Biomass Maps. *Remote Sens. Environ.* **2022**, *272*, 112917. [[CrossRef](#)]

56. Zomer, R.J.; Bossio, D.A.; Trabucco, A.; van Noordwijk, M.; Xu, J.; Zomer, R.J.; Bossio, D.A.; Trabucco, A.; van Noordwijk, M.; Xu, J. Global Carbon Sequestration Potential of Agroforestry and Increased Tree Cover on Agricultural Land. *Circ. Agric. Syst.* **2022**, *2*, 3. [[CrossRef](#)]
57. Fayad, I.; Baghdadi, N.; Alcarde Alvares, C.; Stape, J.L.; Bailly, J.S.; Scolforo, H.F.; Cegatta, I.R.; Zribi, M.; Le Maire, G. Terrain Slope Effect on Forest Height and Wood Volume Estimation from GEDI Data. *Remote Sens.* **2021**, *13*, 2136. [[CrossRef](#)]
58. Wang, Y.; Ni, W.; Sun, G.; Chi, H.; Zhang, Z.; Guo, Z. Slope-Adaptive Waveform Metrics of Large Footprint Lidar for Estimation of Forest Aboveground Biomass. *Remote Sens. Environ.* **2019**, *224*, 386–400. [[CrossRef](#)]
59. Li, M.; Qu, J.J.; Hao, X. Estimating Aboveground Biomass for Different Forest Types Based on Landsat TM Measurements. In Proceedings of the 2009 17th International Conference on Geoinformatics, Fairfax, VA, USA, 12–14 August 2009; pp. 1–6.
60. Li, Y.; Li, C.; Li, M.; Liu, Z. Influence of Variable Selection and Forest Type on Forest Aboveground Biomass Estimation Using Machine Learning Algorithms. *Forests* **2019**, *10*, 1073. [[CrossRef](#)]
61. Saarela, S.; Holm, S.; Healey, S.P.; Andersen, H.-E.; Petersson, H.; Prentius, W.; Patterson, P.L.; Næsset, E.; Gregoire, T.G.; Ståhl, G. Generalized Hierarchical Model-Based Estimation for Aboveground Biomass Assessment Using GEDI and Landsat Data. *Remote Sens.* **2018**, *10*, 1832. [[CrossRef](#)]
62. Yan, S.; He, G.; Zhang, X. Forest Aboveground Biomass Products in China, 2013–2021. *Sci. Data Bank* **2023**, *118*, 103275. [[CrossRef](#)]

Disclaimer/Publisher’s Note: The statements, opinions and data contained in all publications are solely those of the individual author(s) and contributor(s) and not of MDPI and/or the editor(s). MDPI and/or the editor(s) disclaim responsibility for any injury to people or property resulting from any ideas, methods, instructions or products referred to in the content.